Chapter

NON-EQUILIBRIUM SEDIMENT TRANSPORT MODELING — EXTENSIONS AND APPLICATIONS

Weiming Wu[1*], Zhiguo He[2], Qianru Lin[1], Alejandro Sanchez[3], and Reza Marsooli[1]

[1]National Center for Computational Hydroscience and Engineering,
The University of Mississippi, MS 38677, USA
[2]Department of Hydraulic and Ocean Engineeering, Zhejiang University,
Hangzhou 310058, China
[3]Coastal and Hydraulics laboratory, ERDC, U.S. Army Corps of Engineers,
Vicksburg, MS 39180, USA

ABSTRACT

The non-equilibrium sediment transport (NEST) modeling approach has been extended and applied in this chapter to simulate non-cohesive sediment transport induced by rapidly-varying transient flows, by coastal current and waves, in vegetated water bodies, and by overland flow. Even though different flow models are used in these cases, the sediment transport models are similar, with differences in sediment entrainment, adaptation length, and effective diffusivity. In the case of rapidly-varying transient flows, the generalized shallow water flow equations are adopted to consider interactions between flow, sediment transport and bed change. In the coastal context, the flow model adopts the phase-averaged shallow water flow equations with wave-induced radiation stresses coupled with a spectral wave transformation model, and the sediment transport model accounts for sediment entrainment and mixing (diffusion and dispersion) by currents and waves. In the case of vegetated channels, the vegetation drag and inertia forces are considered in the momentum equations and the sediment transport capacity is modified due to vegetation effect. For upland soil erosion, the overland flow is simulated using a 2-D diffusion wave model and the rill/interrill erosion due to raindrop splash and hydraulic shear is considered in the sediment entrainment. In addition, a general NEST model framework has been developed for simulating transport of cohesive/non-cohesive sediment mixtures, taking into account the effects of cohesive sediment flocculation, bed

* Email: wuwm@ncche.olemiss.edu

consolidation and interactions between cohesive and non-cohesive bed materials. Selected test cases demonstrate that the extended NEST models can reasonably reproduce the sediment transport and morphology evolution under these complex flow conditions.

Keywords: Cohesive sediment; non-cohesive sediment; rapidly-varying transient flows; upland soil erosion; vegetation effect; waves

INTRODUCTION

To mitigate natural and man-caused disasters and conserve soil and water resources, better understanding and more reliable prediction of sediment transport by various surface water flows are in high demand. For example, rapidly-varying transient flows, such as dam/levee break flows, storm surge, and tsunami waves, cause intensive erosion over the surface of earthen embankments and barriers and non-equilibrium transport of non-uniform cohesive/non-cohesive sediments in mixed flow regimes. Soil erosion and transport by overland flow involve raindrop splash and rill/interrill/gully erosion. In the coastal environment, sediment transport is affected by both currents and waves. In a vegetated channel, flow is retarded and diverted by vegetation patches and induce different sediment transport and morphological change patterns, whereas in a coastal marshland, vegetation plays an important role in stabilizing the bed against the impacts of surges and waves. In estuaries, reservoirs, lakes and rivers, cohesive and non-cohesive sediment mixtures widely exist and experience complex interactions between sediment size classes. All these sediment transport problems are quite different from the non-cohesive sediment transport under common channel flow conditions described in the previous chapter and require special modeling capabilities. Described in this chapter are several newly developed non-equilibrium sediment transport (NEST) models for these specific applications.

SEDIMENT TRANSPORT UNDER RAPIDLY-VARYING TRANSIENT FLOWS

The morphodynamic processes under actions of rapidly-varying transient flows, such as dam/levee break flows, strong storm surge, and tsunami waves, involve mixed supercritical/subcritical flow regimes, hydraulic jump, strong sediment transport, and rapid bed erosion. Therefore, simulation of flow, sediment transport, and morphology evolution during such events are very challenging. To accurately simulate these processes, the flow model is required to have shock-capturing capabilities. For example, the 1-D and depth-averaged 2-D models often adopt approximate Riemann solvers and TVD (Total Variation Diminishing) schemes (Toro, 2001), while the vertical 2-D and 3-D models use the VOF (volume-of-fluid) method and smooth particle hydrodynamics method to handle the rapidly varying unsteady flows. Moreover, the model should consider the interactions between flow, sediment transport, and bed change. There have been several numerical models in the literature to simulate earthen embankment break flow over movable beds (e.g., Cao et al., 2004; Wang and Bowles, 2006; Faeh, 2007; Wu and Wang, 2007; Roelvink et al., 2009; Wu

et al., 2012). An example of such models is described below, which improves on the model of Wu et al. (2012).

Model Formulations

When the sediment concentration is high, the 3-D continuity equation of water and sediment mixture is given by Equation (1), where t is time, x_i is the ith coordinate (x, y, z for $i = 1, 2, 3$), and u_i is the velocity component of the water and sediment mixture in the ith direction. In Equation (1), ρ is the combined density of water and sediment mixture and is given by $\rho = \rho_w(1-c) + \rho_s c$, where ρ_w and ρ_s are the water and sediment densities, respectively, and c is the sediment concentration by volume.

$$\frac{\partial \rho}{\partial t} + \frac{\partial(\rho u_i)}{\partial x_i} = 0 \tag{1}$$

By using the Reynolds time-averaging, one can have $u_i = \bar{u}_i + u_i'$, $\rho = \bar{\rho} + \rho'$, $c = \bar{c} + c'$, and Equation (1) can be rewritten as Equation (2). In Reynolds time-averaging the instantaneous variables (e.g., u_i) are split into time-averaged quantities (e.g., $\bar{u}_i$) and fluctuating quantities (e.g., u_i'). The fluctuating density, ρ', is related to the fluctuating sediment concentration, c', by $\rho' = (\rho_s - \rho_w)c'$, so that $\overline{\rho' u_i'} = (\rho_s - \rho_w)\overline{c' u_i'}$. The turbulent sediment flux $\overline{c' u_i'}$ is modeled by using the sediment turbulent diffusion concept, yielding the modeled time-averaged continuity equation as given by Equation (3), where ε_s is the sediment turbulent diffusion coefficient.

$$\frac{\partial \bar{\rho}}{\partial t} + \frac{\partial(\bar{\rho}\bar{u}_i)}{\partial x_i} + \frac{\partial(\overline{\rho' u_i'})}{\partial x_i} = 0 \tag{2}$$

$$\frac{\partial \bar{\rho}}{\partial t} + \frac{\partial(\bar{\rho}\bar{u}_i)}{\partial x_i} = (\rho_s - \rho_w)\frac{\partial}{\partial x_i}\left(\varepsilon_s \frac{\partial \bar{c}}{\partial x_i}\right) \tag{3}$$

Integrating Equation (3) over the flow depth leads to the depth-averaged 2-D continuity equation given by Equation (4), where U and V are the depth-averaged flow velocities in x and y directions in the horizontal plane, h is the flow depth, z_b is the bed elevation, C_t is the depth-averaged concentration of sediment (total load), ρ is the density of the water and sediment mixture in the water column determined by $\rho = \rho_w(1 - C_t) + \rho_s C_t$ (where the overbars are omitted for simplicity). The density of the water and sediment mixture in the bed surface layer, denoted as ρ_b, is determined by $\rho_b = \rho_w p_m' + \rho_s(1 - p_m')$, where p_m' is the porosity of bed material in the surface layer. Since Equation (4) governs the continuity of the water and sediment mixture, it accounts for the effect of sediment turbulent diffusion by including the term on its right-hand side.

$$\frac{\partial(\rho h)}{\partial t} + \frac{\partial(\rho U h)}{\partial x} + \frac{\partial(\rho V h)}{\partial y} + \rho_b \frac{\partial z_b}{\partial t} = (\rho_s - \rho_w)\left[\frac{\partial}{\partial x}\left(\varepsilon_s h \frac{\partial C_t}{\partial x}\right) + \frac{\partial}{\partial y}\left(\varepsilon_s h \frac{\partial C_t}{\partial y}\right)\right] \tag{4}$$

Similarly, depth-integrating the time-averaged 3-D momentum equations of the water and sediment mixture, using the hydrostatic pressure assumption, and ignoring some high-order turbulent correlation terms, one can derive the depth-averaged momentum equations of sediment-laden shallow water flow as given by Equations (5) and (6). In these equations, z_s is the water level, n is the Manning roughness coefficient, g is the gravitational acceleration, μ_t is the eddy viscosity, $\tilde{U} = \sqrt{U^2 + V^2}$, and $m_b = \sqrt{1 + \left(\partial z_b / \partial x\right)^2 + \left(\partial z_b / \partial y\right)^2}$, which considers the bed slope effect but can be lumped in the Manning's n coefficient.

$$\begin{aligned} &\frac{\partial}{\partial t}\left(\rho U h\right) + \frac{\partial}{\partial x}\left(\rho U^2 h\right) + \frac{\partial}{\partial y}\left(\rho U V h\right) \\ &= \frac{\partial}{\partial x}\left(\mu_t h \frac{\partial U}{\partial x}\right) + \frac{\partial}{\partial y}\left(\mu_t h \frac{\partial U}{\partial y}\right) - \rho g h \frac{\partial z_s}{\partial x} - \frac{1}{2} g h^2 \frac{\partial \rho}{\partial x} - \rho g \frac{n^2 m_b \tilde{U} U}{h^{1/3}} \end{aligned} \tag{5}$$

$$\begin{aligned} &\frac{\partial}{\partial t}\left(\rho V h\right) + \frac{\partial}{\partial x}\left(\rho U V h\right) + \frac{\partial}{\partial y}\left(\rho V^2 h\right) \\ &= \frac{\partial}{\partial x}\left(\mu_t h \frac{\partial V}{\partial x}\right) + \frac{\partial}{\partial y}\left(\mu_t h \frac{\partial V}{\partial y}\right) - \rho g h \frac{\partial z_s}{\partial y} - \frac{1}{2} g h^2 \frac{\partial \rho}{\partial y} - \rho g \frac{n^2 m_b \tilde{U} V}{h^{1/3}} \end{aligned} \tag{6}$$

The sediment transport and bed change are determined by Equations (7) and (8), where q_{t*} is the capacity or equilibrium transport rate of total-load (bed-material load) sediment, and L_t is the adaptation length of sediment (see the previous chapter). Note that the coefficient m_b considers the lateral erosion along the side slope. It might be lumped in the sediment transport capacity q_{t*}. For many rapidly-varying transient flows, the turbulent stress and diffusion terms in Equations (4)–(7) are usually ignored because they are much smaller than the convection terms.

$$\frac{\partial\left(hC_t\right)}{\partial t} + \frac{\partial\left(hUC_t\right)}{\partial x} + \frac{\partial\left(hVC_t\right)}{\partial y} = \frac{\partial}{\partial x}\left(\varepsilon_s h \frac{\partial C_t}{\partial x}\right) + \frac{\partial}{\partial y}\left(\varepsilon_s h \frac{\partial C_t}{\partial y}\right) - \frac{1}{L_t}\left(\tilde{U} h C_t - m_b q_{t*}\right) \tag{7}$$

$$\left(1 - p'_m\right)\frac{\partial z_b}{\partial t} = \frac{1}{L_t}\left(\tilde{U} h C_t - m_b q_{t*}\right) \tag{8}$$

The sediment transport capacity q_{t*} is determined using the formula of Wu et al. (2000), with the modification suggested by Wu (2007) to consider the effect of gravity on sediment transport over steep slope as explained in the previous chapter. In addition, to consider the effect of sediment concentration, the settling velocity ω_s used in Wu et al. (2000) formula is determined by Richardson and Zaki's (1954) method as $\omega_s = \omega_{s0}\left(1 - C_t\right)^m$, with $m \approx 4$ and ω_{s0} being the settling velocity of single sediment particles in quiescent, distilled water.

Considering nearly vertical sidewalls or banks observed in laboratory and field experiments even for non-cohesive sediment materials, a specially designed avalanching algorithm is adopted here. The non-cohesive slope avalanching algorithm presented by Wu (2007) is modified by specifying two different repose angles for the submerged materials and the emergent materials above the water surface.

By using Equations (7) and (8), Equations (4)–(6) can be reformulated as Equations (9)–(11), respectively. The reformulated continuity equation, Equation (9), is much simpler than

Equation (4). Moreover, the flow density is eliminated from the left-hand sides of Equations (9)–(11), so that the traditional shock-capturing schemes can be more conveniently adopted to solve these equations.

$$\frac{\partial h}{\partial t}+\frac{\partial(Uh)}{\partial x}+\frac{\partial(Uh)}{\partial y}=-\frac{1}{1-p_m'}\frac{\tilde{U}hC_t-m_bq_{t*}}{L_t} \tag{9}$$

$$\begin{aligned}&\frac{\partial(Uh)}{\partial t}+\frac{\partial(U^2h)}{\partial x}+\frac{\partial(UVh)}{\partial y}\\&=\frac{1}{\rho}\left[\frac{\partial}{\partial x}\left(\mu_t h\frac{\partial U}{\partial x}\right)+\frac{\partial}{\partial y}\left(\mu_t h\frac{\partial U}{\partial y}\right)\right]-gh\frac{\partial z_s}{\partial x}-\frac{1}{2}gh^2\frac{1}{\rho}\frac{\partial\rho}{\partial x}-g\frac{n^2m_b\tilde{U}U}{h^{1/3}}\\&+U\frac{\rho_s-\rho_w}{\rho}\left[-\frac{\partial}{\partial x}\left(\varepsilon_s h\frac{\partial C_t}{\partial x}\right)-\frac{\partial}{\partial y}\left(\varepsilon_s h\frac{\partial C_t}{\partial y}\right)+\left(1-\frac{C_t}{1-p_m'}\right)\frac{\tilde{U}hC_t-m_bq_{t*}}{L_t}\right]\end{aligned} \tag{10}$$

$$\begin{aligned}&\frac{\partial(Vh)}{\partial t}+\frac{\partial(UVh)}{\partial x}+\frac{\partial(V^2h)}{\partial y}\\&=\frac{1}{\rho}\left[\frac{\partial}{\partial x}\left(\mu_t h\frac{\partial V}{\partial x}\right)+\frac{\partial}{\partial y}\left(\mu_t h\frac{\partial V}{\partial y}\right)\right]-gh\frac{\partial z_s}{\partial y}-\frac{1}{2}gh^2\frac{1}{\rho}\frac{\partial\rho}{\partial y}-g\frac{n^2m_b\tilde{U}V}{h^{1/3}}\\&+V\frac{\rho_s-\rho_w}{\rho}\left[-\frac{\partial}{\partial x}\left(\varepsilon_s h\frac{\partial C_t}{\partial x}\right)-\frac{\partial}{\partial y}\left(\varepsilon_s h\frac{\partial C_t}{\partial y}\right)+\left(1-\frac{C_t}{1-p_m'}\right)\frac{\tilde{U}hC_t-m_bq_{t*}}{L_t}\right]\end{aligned} \tag{11}$$

Wu et al. (2012) solved Equations (9)–(11) without the turbulent diffusion terms using an explicit finite volume method on a rectangular grid. The HLL approximate Riemann solver (Harten et al., 1983) is used to determine the convective fluxes at cell faces in both *x* and *y* directions. A second-order accurate approximation in space is obtained by reconstructing the left and right states or fluxes using the Monotonic Upstream Scheme for Conservation Laws (MUSCL) (van Leer, 1979). In a later study, Wu and Marsooli (2012) adopted a hybrid approach in which the streamwise convective flux is treated using the HLL solver and MUSCL reconstruction, but the lateral convective flux is determined using the HLPA (Hybrid Linear/Parabolic Approximation) scheme (Zhu, 1991), which has approximately second-order accuracy in space. This hybrid approach has less numerical diffusion than the former approach applying the HLL solver in both *x* and *y* directions.

The water-surface gradient terms in Equations (10) and (11) are treated using the modified center difference scheme suggested by Ying and Wang (2008). If the turbulent diffusion terms are included, they can be discretized using the traditional center difference scheme. The convective flux of sediment at cell faces is determined using the HLPA scheme. The bed change equation, Equation (8), is discretized using a point-wise forward difference scheme. It is well known that oscillations in flow velocity near hydraulic jumps may be generated by the HLL approximate Riemann solver. In order to eliminate the effects of these numerical oscillations on sediment transport and bed changes, the velocity used in the calculation of sediment transport capacity is set as the convective flux averaged from the two cell faces in *x* or *y* direction divided by the flow depth (Wu et al., 2012).

Model Test Examples

The model was tested using a benchmark experiment carried out at Université catholique de Louvain (UCL), Belgium to investigate the two-dimensional morphological evolution of a movable bed under the action of partial dam-break wave (IAHR Working Group, 2012). The flume was 3.6 m wide and about 36 m long, as shown in Figure 1. The partial dam break was represented by rapidly lifting the 1-m wide gate between two impervious blocks. The fixed bed of the flume was covered with an 85 mm thick sand layer extended from 1 m upstream of the dam to 9 m downstream of the gate. The sand was fully saturated before the experiment and had a median diameter of 1.61 mm, a specific gravity of 2.63, and an initial bed porosity of 0.42. The initial water level in the reservoir was 0.47 m above the fixed flume bed, while the downstream was dry bed in this test case. A mesh of 600×140 cells in longitudinal and lateral directions was used to cover the entire flume. The longitudinal and lateral grid spacing was 0.025 m in the movable bed reach near the breach width and increased gradually in the downstream and upstream directions and towards both sidewalls. A constant time step of 0.0005 s was used in this case. The Manning's n in the sand bed was suggested as 0.0165 by the benchmark test (IAHR Working Group, 2012). For the portion of fixed bed, the Manning's n was set as 0.01. The suspended-load adaptation coefficient α was set as 4.0 and the bed-load adaptation length L_b was 0.025 m.

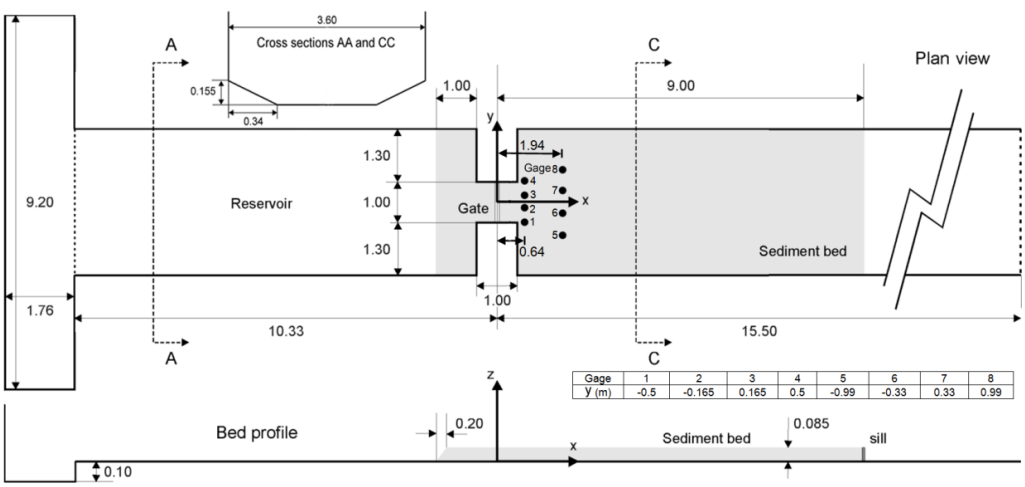

Figure 1. Configurations of the UCL partial dam break experiment (dimension in meters)

Figures 2(a) and (b) compare the calculated and measured bed topographies at the end of the experiment ($t = 20$ s). The measured bed profiles along three longitudinal sections ($y = 0.2$, 0.7 and 1.45 m) at $t = 20$ s are compared with the calculated results in Figure 3. Note that Figure 3 includes bed profiles measured in two experimental runs using the same setup, and difference between the two measurements shows the difficulty of repeating such experiments. Both calculation and measurement showed that significant erosion led to a large scour hole downstream of the dam. Some of the eroded sediment deposited along the sidewalls where hydraulic jumps appeared and downstream of the scour hole. The deposition pattern was controlled by the cross waves generated by the partial dam break, which spread to the sidewalls of the flume and were then reflected from one side to the other side. The calculated scour hole was deeper than the measured one.

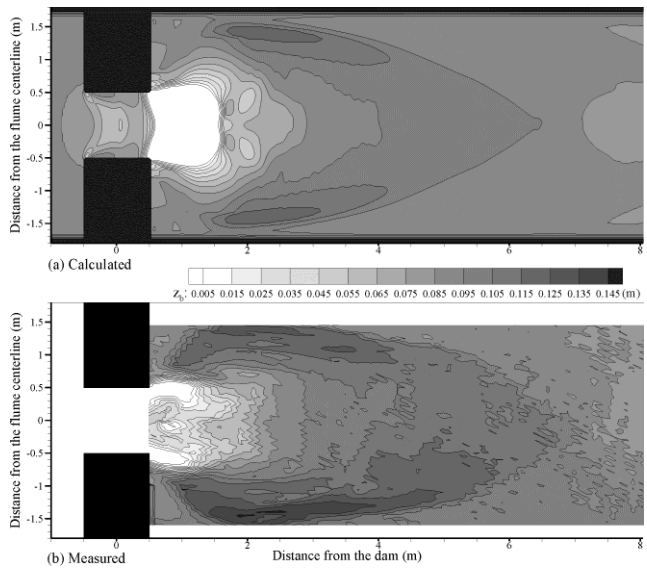

Figure 2. Bed topographies at *t*=20 s: (a) calculated and (b) measured

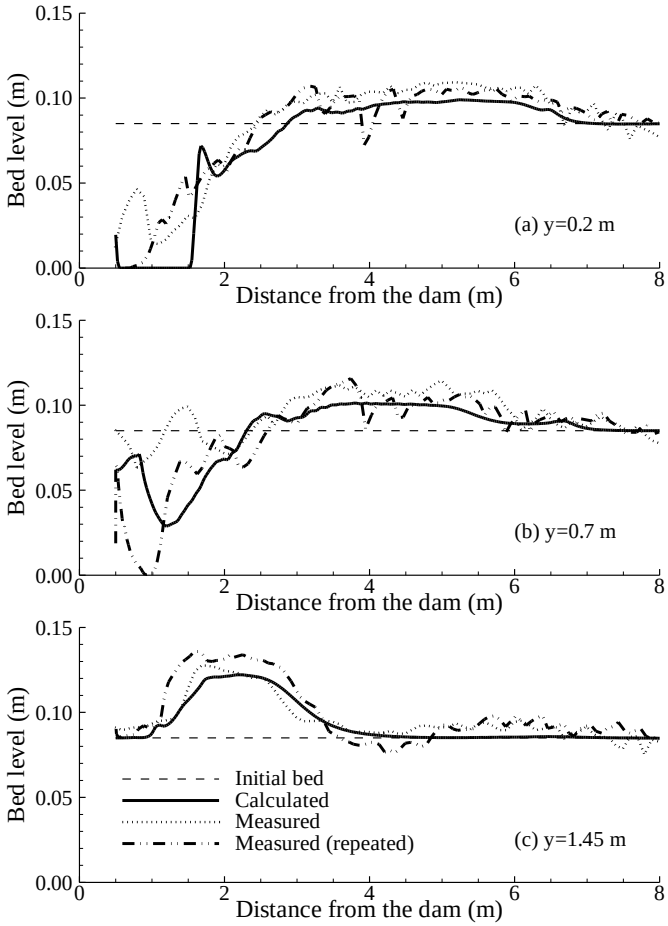

Figure 3. Measured and calculated final bed profiles along three longitudinal sections

Figure 4 shows the measured and simulated time series of water surface elevations (above the fixed flume bottom) at 8 gage points marked in Figure 1. The variations of water surface at Gages 1 and 4 have the same trend, due to almost symmetric flow, sediment transport, and bed change patterns about the channel centerline observed by the model simulation. Similar trends can also be observed between Gages 2 and 3, between Gages 5 and 8, and between Gages 6 and 7. The calculated water levels at Gages 1 and 4 are lower than the measured ones. This may be due to strong 3-D features of the flow near the two corners of sudden expansion of the flume width, as well as the over predicted erosion there.

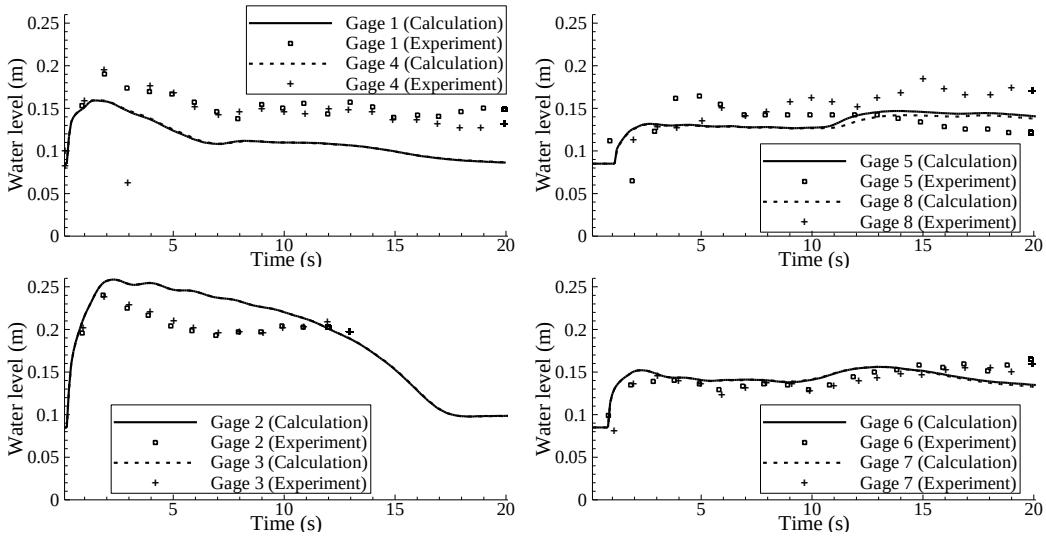

Figure 4. Measured and calculated water surface variations with time at 8 gage points

The model was also tested using the IMPACT laboratory experiments carried out by HR Wallingford, UK (Morris et al., 2009). The flume was 50 m long and 10 m wide. A model dam of 0.5 m in height was located at about 36 m downstream of the flume entrance. It had a crest width of 0.2 m and up/downstream slopes of 1V:1.7H. A wide grading and a narrow grading sediment mixture were tested in the experiment. The two sediment mixture gradations had the same median diameter of 0.25 mm. A uniform mesh consisting of 1000×200 nodes in longitudinal and lateral directions was used in the simulation. The dam material porosity was estimated as 0.36, and the Manning's n was estimated as 0.018. The initial pilot channel was 0.02 m deep and 0.152 m wide. The repose angle of the bed material was set to be 31° in the submerged condition and about 80° in the emergent condition. The inflow discharge of 0.07 m^3/s was specified at the flume entrance. Calibration showed that a constant L_t of 0.07 m gave reasonable results in this case.

Figure 5 shows the calculated bed topography and flow pattern at the peak breach flow. At the downstream of the breach, the flow spread laterally and small bed forms or undulations appeared on both sides of the flow. The simulated breach exhibits a "bell mouth" weir flow and topography, as observed in the experiment. Figure 6 compares the measured and calculated breach flow discharges variation with time, and Figure 7 compares the measured and calculated breach widths and headwater levels. The two figures show that the model

predicted a steeper rising limb of breach flow hydrograph, a slower tailing of reservoir water level and a faster widening process than the experiment. The calculation results agree generally well with the measured data. In particular, the peak breach flow discharge and the final breach width are well predicted by the model.

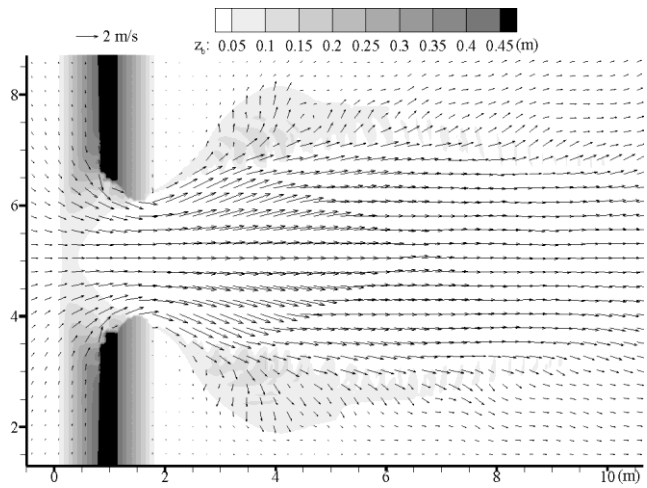

Figure 5. Simulated flow pattern and bed topography at the peak breach flow

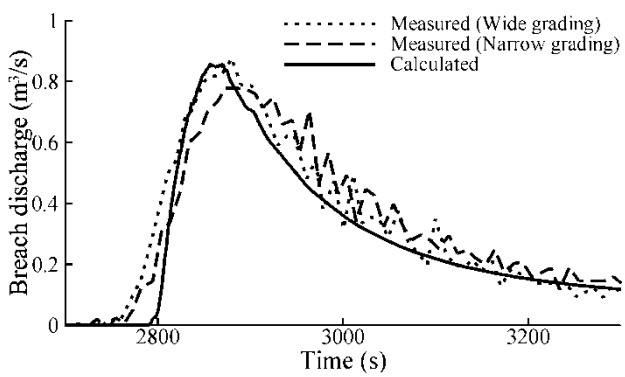

Figure 6. Measured and simulated breach flow discharges

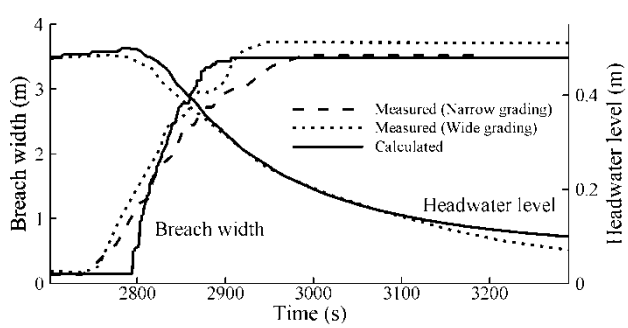

Figure 7. Measured and simulated breach widths and headwater levels

SEDIMENT TRANSPORT BY CURRENTS AND WAVES

In the context of coastal environment, because the multiple interacting forces (waves, wind, tide, river flow, density current, etc.) exhibit a wide range of spatial and temporal scales, the complex costal physical processes are quantitatively not well understood. Traditionally, most coastal sediment transport models adopt the equilibrium transport concept. The following section presents an application of the NEST model in the Coastal Modeling System (CMS) as illustrated by Sanchez and Wu (2011).

Model Formulations

The CMS, developed under the U. S. Army Corps of Engineers' Coastal Inlets Research Program (CIRP), is designed for practical applications in navigation channel performance evaluation and sediment management near coastal inlets and adjacent beaches. It is a phase-averaged model, in which the circulation model computes the unsteady water level and current velocity fields by solving the phase-averaged, depth-averaged 2-D shallow water flow equations on a non-uniform or quadtree Cartesian grid with an explicit and implicit finite volume scheme (Buttolph et al., 2006; Wu et al., 2011). The model can simulate tide, wind and wave driven currents, and includes the Coriolis force, wind stress, bottom friction, and wave radiation stresses. The phase-averaged 2-D shallow water flow equations can be written as Equations (11)–(13) of the previous chapter. In these equations D_{ij} $(i, j = x, y)$ represents the wave-driven radiation stresses and is given by Equation (12), where E is the wave energy density, f is the wave frequency, θ is the wave direction, w_i is the wave unit vector $(\cos\theta, \sin\theta)$, $n_g = 0.5(1 + 2kh/\sinh 2kh)$, and k is the wave number. The bed shear stresses experienced by the currents in the case where both waves and currents coexist are given by Equations (13) and (14), where U_{wm} is the maximum orbital bottom velocity of waves and $c_f = gn^2/h^{1/3}$.

$$D_{ij} = \iint E(f,\theta)\left[n_g w_i w_j + \delta_{ij}\left(n_g - 0.5\right)\right] df d\theta \tag{12}$$

$$\tau_{bx} = c_f \rho \left(U^2 + V^2 + 0.5U_{wm}^2\right)^{1/2} U \tag{13}$$

$$\tau_{by} = c_f \rho \left(U^2 + V^2 + 0.5U_{wm}^2\right)^{1/2} V \tag{14}$$

The wave characteristics are determined using a spectral wave transformation model that solves the steady-state wave-action balance equation on a non-uniform Cartesian grid with a finite difference scheme. It considers wind wave generation and growth, diffraction, reflection, dissipation due to bottom friction, white capping and breaking, wave-wave and wave-current interactions, wave runup, wave setup, and wave transmission through structures (Lin et al., 2008). The sediment transport model calculates the depth-averaged 2-D non-equilibrium transport of total load and the resulting bed change using Equations (15) and (16), where r_s is the ratio of suspended load to total load, U_c is the current speed, D_s is the empirical coefficient for the effect of bed slope on bed load, and the subscript j denotes the index of horizontal coordinates x and y.

$$\frac{\partial}{\partial t}\left(\frac{hC_{tk}}{\beta_{tk}}\right)+\frac{\partial\left(U_j hC_{tk}\right)}{\partial x_j}=\frac{\partial}{\partial x_j}\left[\varepsilon_s h\frac{\partial\left(r_s C_{tk}\right)}{\partial x_j}\right]+\alpha_t\omega_{sk}\left(C_{t*k}-C_{tk}\right) \tag{15}$$

$$\left(1-p'_m\right)\frac{\partial z_b}{\partial t}=\sum_{k=1}^{N}\alpha_t\omega_{sk}\left(C_{t*k}-C_{tk}\right)+\frac{\partial}{\partial x_j}\left[D_s U_c h\left(1-r_s\right)C_t\frac{\partial z_b}{\partial x_j}\right] \tag{16}$$

Note that the effect of bed slope on bed-load transport is taken into account by the last term in Equation (16), whereas this is accounted for through the transport direction cosines α_{bx} and α_{by} in Equation (24) in the previous chapter. The approach of Equation (16) is found to be more stable, but with a loosely defined coefficient D_s. Watanabe (1985) used $D_s=10$ based on a free-body diagram of the grain in a sloping bed. Struiksma et al. (1985) used $D_s=4$. Later studies, such as Larson et al. (2003) and Karambas (2003), reported good results with $D_s=2$. Sanchez and Wu (2011) used a value of about 1 to avoid over-smoothing the morphology change. In practice, D_s may be a function of the flow and sediment characteristics and vary from site to site.

The effective sediment diffusivity ε_s is related to the eddy viscosity ν_t by $\varepsilon_s=\nu_t/\sigma_c$, in which σ_c is the Schmidt number. The eddy viscosity includes the effects of currents, waves, and wave breaking as given by Equation (17), where $\nu_{t,c}$ is the eddy viscosity due to currents and can be determined using several turbulence models, such as the depth-averaged parabolic model and the modified mixing-length model, Λ is an empirical coefficient representing the lateral wave mixing strength, H is the wave height, D_b is the energy dissipation rate due to wave breaking, and k_b is an empirical coefficient. The second and third terms on the right-hand side of Equation (17) account for the effects of waves and wave breaking, respectively.

$$\nu_t=\nu_{t,c}+\Lambda U_{wm}H+k_b\left(\frac{D_b}{\rho}\right)^{1/3}h \tag{17}$$

The sediment transport capacity C_{t*k} under currents and waves is significantly affected by interactions between currents and waves. The available formulas for determining C_{t*k} include Watanabe (1987), Soulsby (1997), Lund-CIRP (Camenen and Larson 2007), and van Rijn (2007a, b). Wu and Lin (2012) extended the non-uniform sediment transport capacity formula of Wu et al. (2000) to the cases where both waves and currents exist.

Model Test Example

The model was tested against many laboratory and field case studies (Sanchez and Wu, 2011; Sanchez et al., 2011). One of the field cases was the application in the Shinnecock Inlet on Long Island, NY. It is a mixed-energy, wave dominated inlet, with mainly semidiurnal tide with an average spring tidal range of 1.1 m. The Shinnecock Bay has water depths typically less than 2 m and a tidal prism of 3.29×0^7 m^3. Typical wave conditions are from the southeast with wave heights of 1 m and periods of 7 s, while northeast storms and hurricanes can produce wave heights in excess of 4 m with periods of 12–14 s (Buonaiuto and Militello, 2003). The simulation covered the time period between August 13, 1997 and May 28, 1998. Figure 8 shows the computational domain with initial bathymetry of 1997. The grid for flow

computation had 49,780 cells and a variable grid resolution between 15 and 100 m. The sediment size ranged from 0.125 mm offshore and inside the bay to 2 mm in the inlet, but the predominant size was 0.5 mm, which was used in the simulation. The sediment transport capacity was calculated with the Watanabe (1987) equation adjusted by multiplying a factor of 0.25. The sediment adaptation length was given as 20 m, and the bed slope coefficient D_s was 1.0.

The calculated longshore sediment transport rate was 133,000 yd^3/yr, which was within the range of 110,000–190,000 yd^3/yr reported by Rosati et al. (1999). Figure 9 shows the measured and computed morphology changes. Qualitatively, the results showed several features in common such as deposition on the peripheral of the ebb shoal, erosion at both the east and west bypass bars, erosion of the eastern portion of the south bypass bar, and accretion in the deposition basin. Quantitatively, the morphodynamic model correctly predicted either an erosional or depositional trend at approximately 66% of the computational cells (Sanchez and Wu, 2011).

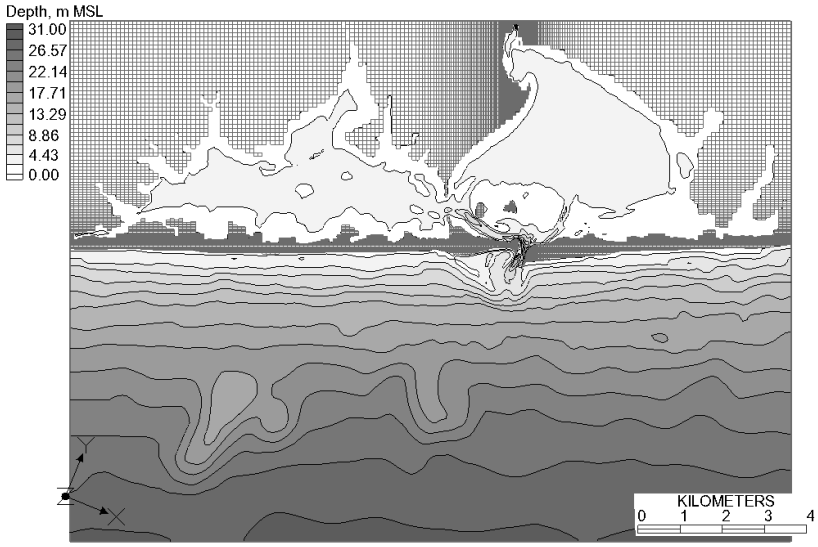

Figure 8. Computational domain with initial bathymetry for 1997 (square cells represent inactive land cells)

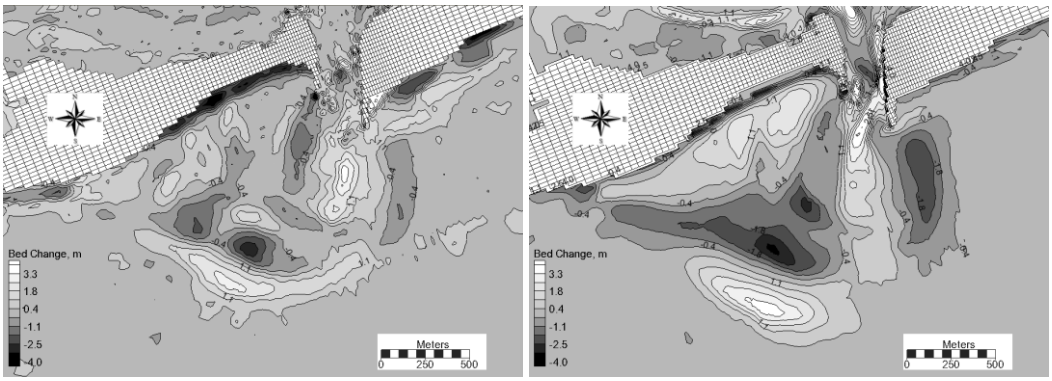

Figure 9. (left) Measured and (right) simulated morphology changes between August 1997 and May 1998 (Sanchez and Wu, 2011)

SEDIMENT TRANSPORT IN VEGETATED CHANNELS

Governing Equations

Flow through vegetation usually is unsteady and turbulent, but the mostly considered flow properties in practice are the time- and space-averaged behaviors rather than the detailed instantaneous flow features around individual vegetation. By double-averaging the Navier-Stokes equations in time and space, one can derive the governing equations of free-surface flow through vegetation (Nikora et al., 2007; Lopez and Garcia, 2001). Based on the hydrostatic pressure assumption, further depth-averaging (Wu and Wang, 2004a) the double-averaged 3-D Navier-Stokes equations leads to the shallow water equations with vegetation effects as given by Equations (18)–(20), where c_v is the depth-averaged volumetric concentration of vegetation, and F_{dx} and F_{dy} are the x- and y-components of the drag force and inertia force on vegetation exerted by the flow. These forces, as defined by Morison et al. (1950), are given by Equation (21), where C_d is the drag coefficient of vegetation, C_M is the inertia coefficient of about 2, ρ is the water density, N_v is the vegetation density defined as number of vegetation elements per unit horizontal (bed) area, A_v is the projected area defined as the frontal area of a vegetation element projected to the plane normal to the stream-wise flow direction, V_v is the volume of a vegetation element, $\vec{U}_v$ is the vector of flow velocity acting on the vegetation element, and $|U_v|$ (or simply written as U_v) is the magnitude of $\vec{U}_v$. For emergent vegetation, $\vec{U}_v$ is the depth-averaged flow velocity $\vec{U}$, while for submerged vegetation, $\vec{U}_v$ should be the velocity averaged only over the vegetation layer, as shown in Figure 10.

$$\frac{\partial\left[(1-c_v)h\right]}{\partial t}+\frac{\partial\left[(1-c_v)hU\right]}{\partial x}+\frac{\partial\left[(1-c_v)hV\right]}{\partial y}=0 \tag{18}$$

$$\begin{aligned}&\frac{\partial\left[(1-c_v)hU\right]}{\partial t}+\frac{\partial\left[(1-c_v)hU^2\right]}{\partial x}+\frac{\partial\left[(1-c_v)hUV\right]}{\partial y}+g(1-c_v)h\frac{\partial z_s}{\partial x}\\&=\frac{1}{\rho}\frac{\partial\left[(1-c_v)hT_{xx}\right]}{\partial x}+\frac{1}{\rho}\frac{\partial\left[(1-c_v)hT_{xy}\right]}{\partial y}-(1-c_v)\frac{\tau_{bx}}{\rho}-\frac{1}{\rho}F_{dx}\end{aligned} \tag{19}$$

$$\begin{aligned}&\frac{\partial\left[(1-c_v)hV\right]}{\partial t}+\frac{\partial\left[(1-c_v)hUV\right]}{\partial x}+\frac{\partial\left[(1-c_v)hV^2\right]}{\partial y}+g(1-c_v)h\frac{\partial z_s}{\partial y}\\&=\frac{1}{\rho}\frac{\partial\left[(1-c_v)hT_{yx}\right]}{\partial x}+\frac{1}{\rho}\frac{\partial\left[(1-c_v)hT_{yy}\right]}{\partial y}-(1-c_v)\frac{\tau_{by}}{\rho}-\frac{1}{\rho}F_{dy}\end{aligned} \tag{20}$$

$$\vec{F}_d=\frac{1}{2}C_d\rho N_v A_v|U_v|\vec{U}_v+\rho C_M N_v V_v\frac{\partial\vec{U}_v}{\partial t} \tag{21}$$

The depth-averaged 2-D transport equation of suspended load in vegetated channels is given by Equation (22), where C_k is the depth-averaged concentration of the kth size class of suspended load. The vegetation density term $1-c_v$ also appears in the double-averaged 3-D Navier-Stokes equations and suspended-load transport equation (Wu, 2007). The transport equation of bed load in vegetated channels is given by Equation (23), where c_{vb} is the volumetric concentration of vegetation in the bed-load layer.

$$\frac{\partial\left[(1-c_v)hC_k/\beta_{sk}\right]}{\partial t}+\frac{\partial\left[(1-c_v)hUC_k\right]}{\partial x}+\frac{\partial\left[(1-c_v)hVC_k\right]}{\partial y}$$
$$=\frac{\partial}{\partial x}\left[(1-c_v)\varepsilon_s h\frac{\partial C_k}{\partial x}\right]+\frac{\partial}{\partial y}\left[(1-c_v)\varepsilon_s h\frac{\partial C_k}{\partial y}\right]+\alpha\omega_{sk}(1-c_v)(C_{*k}-C_k) \tag{22}$$

$$\frac{\partial\left[(1-c_{vb})q_{bk}/u_{bk}\right]}{\partial t}+\frac{\partial\left[\alpha_{bx}(1-c_{vb})q_{bk}\right]}{\partial x}+\frac{\partial\left[\alpha_{by}(1-c_{vb})q_{bk}\right]}{\partial y}=\frac{1}{L}(1-c_{vb})(q_{b*k}-q_{bk}) \tag{23}$$

The bed change can be determined by Equation (24), where c_{vbed} is the volumetric concentration of vegetation at the bed surface.

$$(1-p_m')(1-c_{vbed})\left(\frac{\partial z_b}{\partial t}\right)_k=\alpha\omega_{sk}(1-c_v)(C_{*k}-C_k)+\frac{1}{L}(1-c_{vb})(q_{b*k}-q_{bk}) \tag{24}$$

In the case of low vegetation density, Equations (18)–(20), (22) and (23) reduce to the 2-D flow and sediment transport equations expressed in Equations (11)–(13), (15) and (24) in the previous chapter, with the drag force and inertia force added in the momentum equations.

The drag coefficient C_d is the key parameter in the vegetation effect model. It is related to vegetation properties and flow conditions. The turbulent stresses can be determined using the modified mixing-length model (Wu and Wang, 2004a) and $k-\varepsilon$ turbulence model (Lopez and Garcia, 2001). The turbulence generated by vegetation needs to be considered in the k and ε equations. For details refer to Wu (2007).

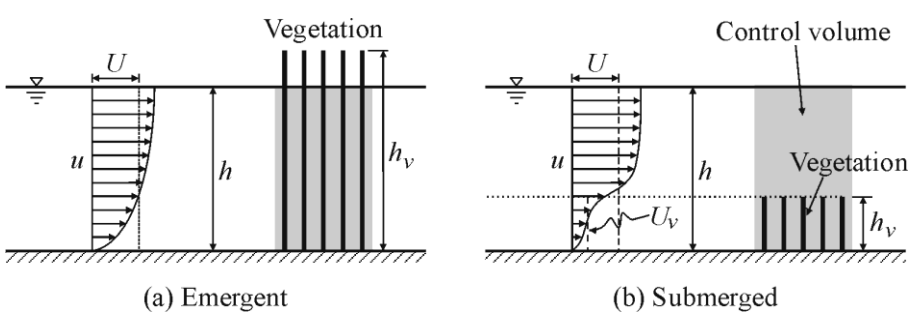

Figure 10. Vegetation in open channels (side view)

Sediment Transport Capacity Formulas

Sediment transport capacity in vegetated channels is affected by vegetation. Okabe et al. (1997), Jordanova and James (2003), and Wu et al. (2005) found that the bed-load transport is mainly related to the bed shear rather than the drag force exerted on vegetation elements. If the effective bed shear is used, some existing empirical formulas developed for the bed-load

transport in non-vegetated channels can be extended to vegetated channels. Jordanova and James (2003) experimentally investigated the bed-load transport in a flume covered with uniformly distributed vegetation. They used the method of Li and Shen (1973) to determine the effective bed shear, and proposed a simple empirical formula. Okabe et al. (1997) used the $k-\varepsilon$ turbulence model to compute the effective bed shear stress, and found that the Ashida-Michiue (1972) formula can be used to determine the bed-load transport rate in vegetated channels. Wu et al. (2005) and Wu and He (2009) found that the formula of Wu et al. (2000) is applicable for the bed-load transport in vegetated channels if the approach of Barfield et al. (1979) is used to determine the effective bed shear stress as given by Equation (25), where S is the bed slope or energy slope, γ is the specific weight of water, and $R_s = h\,l_n \big/ \left(2h + l_n\right)$, in which h is the flow depth, and l_n is the lateral spacing between vegetation elements.

$$\tau_b = \gamma R_s S \tag{25}$$

The suspended-load transport in vegetated channels has not been extensively investigated. As vegetation may reduce the mean flow velocity significantly but intensify the turbulence in a vegetated zone, the effect of vegetation on suspended-load transport is more complex. More experimental and theoretical studies are needed to quantify this effect. As an approximation, one may apply some existing suspended load formulas established under non-vegetated conditions to vegetated channels. Certainly, this application should be carried out with caution.

Model Test Examples

The depth-averaged 2-D model of rapidly-varying transient flows described in the previous section has been extended to flow in vegetated waters by adding the drag and inertia forces in the momentum equations, Equations (10) and (11). The model has been tested using Bennett and Alonso's (2003) experiments on morphodynamics near alternate vegetation zones in an open channel. Two experiment runs were conducted in a laboratory flume that had a preformed trapezoidal cross-section with side slopes of 34°, and two alternate vegetation zones separated by a distance of 1.5 m, as shown in Figure 11. The vegetation zones were 0.49 m long and 0.245 m wide rectangles in experimental run 1 and semi-circles with radii of 0.245 m in run 2. In both experimental runs, the vegetation elements were emergent, rigid, and in a staggered pattern, and had a stem diameter of 4.8 mm and a density of 2500 units/m^2. The sediment size was 0.8 mm. The computational mesh is uniform, with $\Delta x = 0.041$ m and $\Delta y = 0.016$ m, as shown in Figure 11. The Manning's roughness coefficient is adjusted to 0.028, which yields a uniform flow in the absence of vegetation. The drag coefficient C_d is set as 2.0. The sediment adaptation length is determined using Equation (32) in the previous chapter, with $L_b = 0.025$ m and $\alpha = 4$.

In this test case, the effects of sediment concentration and bed changes on the flow can be ignored because the flow is subcritical and the sediment transport is weak. The bank slope is high, so that the effect of gravity on bed-load transport on the slope needs to be considered. This is done using Equation (16), with $D_s = 10$. As the sediment particles were non-cohesive, the model simulates the bank erosion and retreatment by applying repose angle to the bank

slope. The wetted and dry repose angles are set as 34° and 50°, respectively, as explained in the previous chapter.

Figures 12 and 13 show the comparison of the measured and predicted changes in bed and bank topography near the second vegetation zone in an elapsed time of 110 minutes. Deposition occurs in and near the vegetation zone, whereas erosion occurs in the area away from the vegetation zones, resulting in a meandering channel planform. The channel erosion and deposition magnitudes and distributions are predicted reasonably well. The erosion and deposition magnitudes near the rectangular vegetation zone are larger than those near the semi-circular vegetation zone.

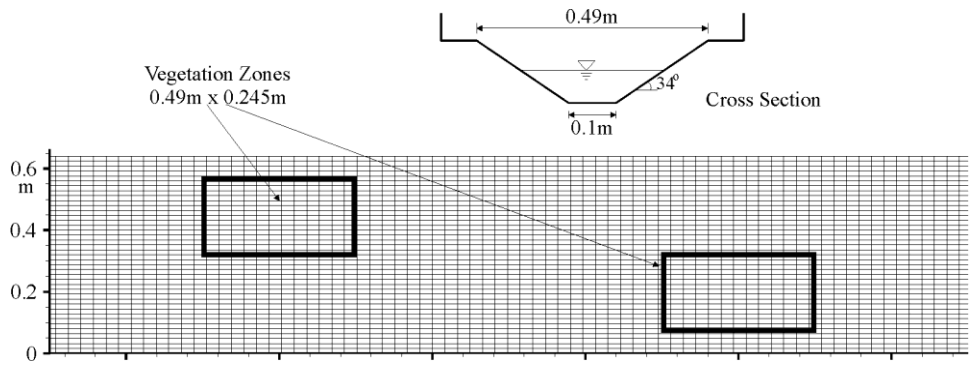

Figure 11. Mesh and sketch of the experiments of Bennett and Alonso (2003)

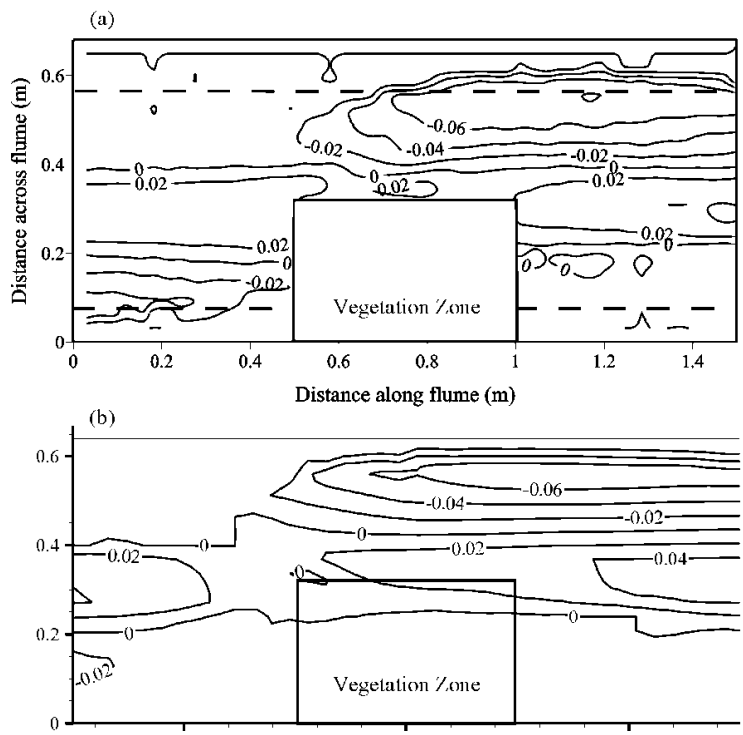

Figure 12. Changes in bed topography due to rectangular vegetation zones: (a) Measured by Bennett and Alonso (2003); (b) Simulated. (Dashed lines show the location of the channel top width, and rectangles show the extent of the vegetation zone)

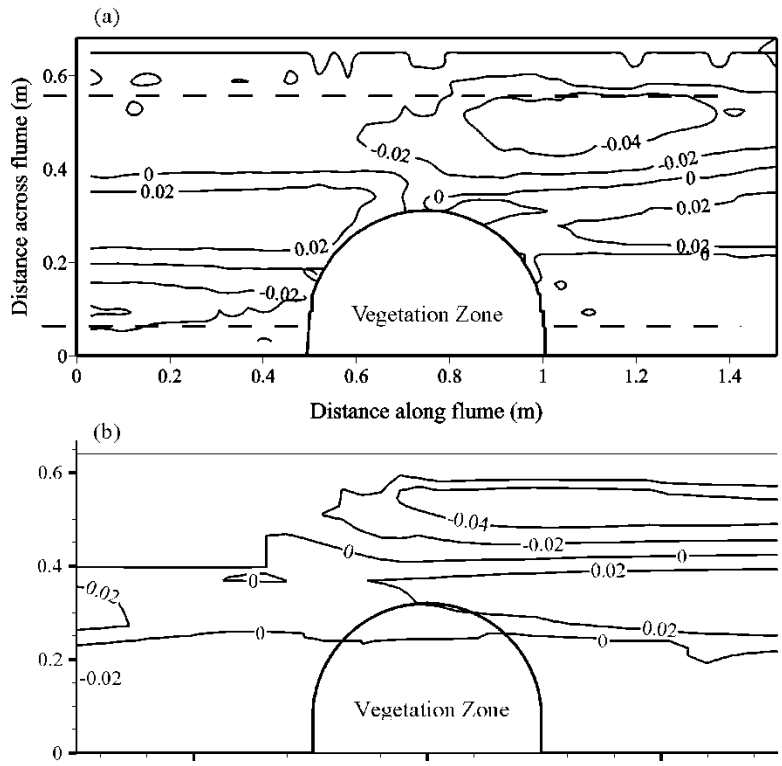

Figure 13. Changes in bed topography due to semi-circular vegetation zones: (a) Measured by Bennett and Alonso (2003); (b) Simulated. (Dashed lines show the location of the channel top width, and semi-circles show the extent of the vegetation zone)

SOIL EROSION AND TRANSPORT BY UPLAND FLOW

To investigate the complex hydrological, morphodynamic, and environmental processes in watersheds, a physically-based integrated 2-D surface and 3-D subsurface model for flow, soil erosion and transport, and contaminant transport was developed by He et al. (2009). The model simulates the rainfall-induced surface flow by solving the depth-averaged 2-D diffusion wave equation and the variably saturated subsurface flow by solving the 3-D mixed-form Richards equation. The surface and subsurface flow equations are coupled using the continuity conditions of pressure and exchange flux at the ground surface. The NEST model is applied to compute the non-uniform soil erosion and transport in upland fields, considering detachments by rain splash and hydraulic erosion driven by surface flow. The integrated 2-D surface and 3-D subsurface contaminant transport model takes into account the contaminant changes due to sediment sorption and desorption, as well as exchanges between surface and subsurface domains due to infiltration, diffusion, and bed change. The 2-D soil erosion and transport model component is briefly presented here.

Model Formulations

When inertia is not important, the surface flow can be described using the depth-averaged 2-D diffusion wave equation as suggested by Di Giammarco et al. (1996) and given by Equation (26), where H_s is the water surface elevation (m), which is the sum of surface water depth h (m) and bed elevation z_b (m), q_r is the rainfall rate (m/s), q_e is the water exchange rate with subsurface (m/s), q_o includes other sources/sinks (m/s), and k_{ox} and k_{oy} are the diffusion coefficients (m^2/s) determined by $k_{ox} = h^{5/3} \big/ \left(n_x^2 \Omega^{1/2}\right)$ and $k_{oy} = h^{5/3} \big/ \left(n_y^2 \Omega^{1/2}\right)$ with n_x and n_y being the Manning roughness coefficients (s/m$^{1/3}$) in x and y directions (anisotropic surface roughness), respectively, and Ω is the friction or energy slope operator (m$^{2/3}$/s^2), approximated as $\Omega = \left[\left(\partial H_s/\partial x\right)^2 \big/ n_x^4 + \left(\partial H_s/\partial y\right)^2 \big/ n_y^4\right]^{\frac{1}{2}}$. In the event of a zero fluid potential gradient, a small number (e.g., 10^{-8} to 10^{-10}) is used for Ω to avoid a division by zero in the expressions of diffusion coefficients.

$$\frac{\partial H_s}{\partial t} = \frac{\partial}{\partial x}\left(k_{ox}\frac{\partial H_s}{\partial x}\right) + \frac{\partial}{\partial y}\left(k_{oy}\frac{\partial H_s}{\partial y}\right) + q_o + q_r + q_e \tag{26}$$

On the upland area, raindrops first generate interrill (sheet) erosion, and then with increasing flux overland flow may cause rill erosion. The soil erosion and transport by overland flow can be described by the 2-D depth-averaged NEST equation as described by Equation (27). The bed change rate due to size class k is determined using Equation (28), where C_{tk} is the depth-averaged concentration of the kth size class of total-load sediment, D_{ik} is the interrill erosion rate, and D_{fk} is the rill erosion rate. The bed material sorting is simulated using the multiple-layer approach presented in the previous chapter.

$$\frac{\partial\left(hC_{tk}\right)}{\partial t} + \frac{\partial\left(UhC_{tk}\right)}{\partial x} + \frac{\partial\left(VhC_{tk}\right)}{\partial y} = \frac{\partial}{\partial x}\left(\varepsilon_s h\frac{\partial C_{tk}}{\partial x}\right) + \frac{\partial}{\partial y}\left(\varepsilon_s h\frac{\partial C_{tk}}{\partial y}\right) + D_{ik} + D_{fk} \tag{27}$$

$$\left(1 - p_m'\right)\left(\frac{\partial z_b}{\partial t}\right)_k = -D_{ik} - D_{fk} \tag{28}$$

Interrill erosion depends on soil properties, surface slope, vegetation, land use, rainfall intensity, and hydraulic factors of runoff. Soil detachment by raindrop impact and splash is the main source of interrill erosion. The interrill erosion rate is determined with the Xiang (2002) formula, which was derived using the grey relation and regression analysis based on experimental data and is illustrated by Equation (29), where d_k is the diameter of k size soil particles, S_0 is the bed slope, p_{bk} is the bed material gradation in the surface layer, and R_c is the saturated sediment transport capacity of interrill. Low's (1989) formula, as given by Equation (30), is used to determine the saturated sediment transport capacity of interrill, where $\Theta = \tau / [(\rho_s - \rho) g d_k]$, $\Theta_c = \tau_c / [(\rho_s - \rho) g d_k]$, τ is the flow shear stress, τ_c is the critical shear stress, and S_f is the energy slope.

$$\frac{D_{ik} d_k}{R_c} = 1.8 \times 10^{-9}\left(\frac{h}{d_k}\right)^{1.5}\left(1.05 - 0.85 e^{-4S_0}\right) p_{bk} \tag{29}$$

$$R_c = \frac{6.42}{\left(\rho_s/\rho - 1\right)^{0.5}}\left(\Theta - \Theta_c\right) d_k S_f^{0.6} \tilde{U} \rho_s \tag{30}$$

Sediment transport in rills is similar to that in open channels. Based on the non-equilibrium concept, the rill erosion and/or deposition by overland flow are estimated as given by Equation (31). In the equation, q_{t*k} is the sediment transport capacity of rill flow calculated by Yalin's (1963) formula, q_{tk} is the actual sediment transport rate, and L_t is the adaptation length related to the adaptation coefficient α_t by $L_t = Uh/(\alpha_t \omega_{s0})$.

$$D_{fk} = \frac{1}{L_t}\left(q_{t*k} - q_{tk}\right) \tag{31}$$

Model Test Examples

The model has been verified and validated using analytical solutions, laboratory data and field data (He et al., 2009). One case is the field erosion experiment of Barfield et al. (1983) on a plot of 4.6 m × 22.1 m with a slope of 0.09. The bed material in the experiment was tilled and wet topsoil with a median grain size $d_{50} = 0.06$ mm. The rainfall intensity used in the simulation was 61 mm/h, lasting for 30 min. The flow and sediment discharges measured at the downstream end of the plot were compared with the model results. The total simulation time was 40 min and the time step was 3 sec. The computational mesh was 20×10 in length and width. A constant infiltration rate of 4.5 mm/h was used in the simulation due to the lack of soil properties. As shown in Figure 14, one can see that the model provided a good prediction for both flow and sediment discharges.

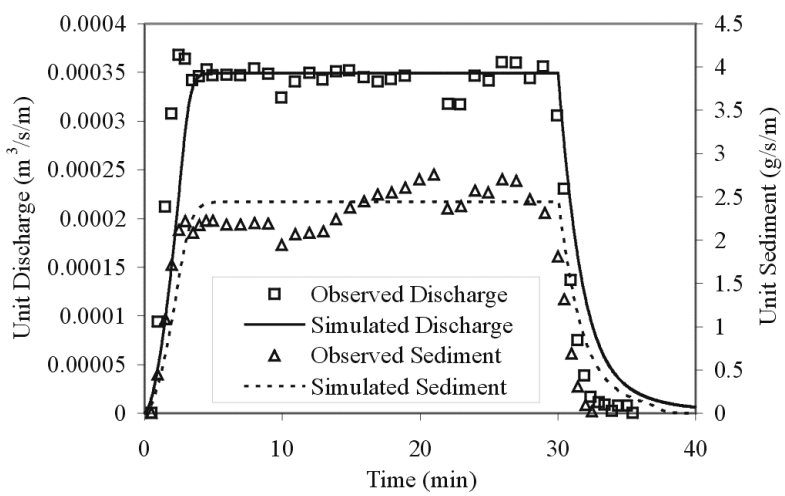

Figure 14. Predicted hydrograph and sedimentograph with observed data of Barfield et al. (1983)

The other test example was simulation of rainfall-runoff, soil erosion and transport, and contaminant transport in the Deep Hollow Lake watershed, located in the northern Mississippi, U.S.A. The watershed is about 202 ha, covered with cotton and soybean fields and wood area. The oxbow lake has a length of ~1 km and a width of ~100 m. Upland elevations within the watershed range from 35 to 39 m above the sea level. Water depth in the lake ranges from 0.5 to 2.6 m, with the greatest depth in the middle. Two gauging stations,

DH1 and DH2, were installed at two of the inlets of the lake by the U.S. Geological Survey. Within the watershed, the surficial clay layer varies from 2.4 to 4.6 m while the underlying silty-sand layer is approximately 33.5 m thick.

The model was applied to simulate the storm event of February 10, 1998. The computational mesh size was 380×252×50 in length, width, and depth. The horizontal grid spacing $(\Delta x, \Delta y)$ was 5 m, while the vertical grid spacing (Δz) was 0.2 m. The time step was 1.5 sec. The soil mixture was divided into three size classes of clay (0.0017 mm), silt (0.027 mm), and sand (0.805 mm). The Manning's roughness coefficient n had values of 0.1, 0.05, 0.04, 0.08, and 0.01 for forest, cotton, soybean, pasture, and water, respectively. The adaptation coefficient α_t was calibrated as 0.5. The predicted average sediment concentration during the storm at Station DH1 was 1686.1 mg/l, which was very close to the observed value of 1620.0 mg/l. Figure 15 shows the predicted and observed flow and sediment discharges at Station DH2 during the storm event. Although the sediment rate was slightly underestimated at the beginning of rainfall, the peak value and trend were predicted generally well.

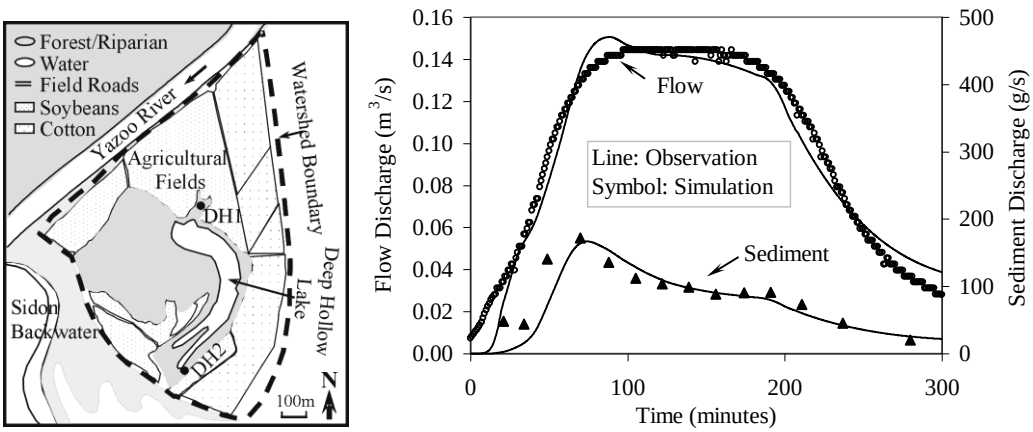

Figure 15. (left) the Deep Hollow Lake Watershed and (right) Flow and Sediment Discharges at DH2 on 02/10/98 (He et al., 2009)

TRANSPORT OF COHESIVE/NON-COHESIVE SEDIMENT MIXTURES

Sediments in natural surface waters can be classified as cohesive (clay and fine silt) and non-cohesive (coarse silt, sand, gravel and cobble). Non-cohesive sediments transport in disperse particles, whereas cohesive sediments transport mainly in flocs. Because the magnitude of electrostatic forces acting among these particles is comparable to or larger than that of the gravitational forces, the fine particles may stick together forming aggregates (or flocs) when they collide due to Brownian motions, turbulent mixing, and/or differential settling. On the other hand, during the transport process, larger flocs may be disaggregated into finer flocs and single particles due to high shear or large eddy ejection and sweeping. Therefore, the cohesive sediment flocs behave much differently from the non-cohesive single particles. Meanwhile, the settled cohesive deposits on the bed may consolidate due to the gravity and the overlying water pressure.

Modeling of either non-cohesive or cohesive sediment transport has been widely investigated (Wu, 2007). However, how to simulate transport of non-cohesive and cohesive sediment mixtures has been rarely studied, but have gained more and more attention recently (Ziegler and Nisbet, 1995; Lin, 2010). It has been recognized that when the fraction of fine-grained sediments is larger than about 10%, sediment mixtures consisting of cohesive and non-cohesive particles may exhibit cohesive properties and undergo very complicated transport processes. Flocculation of the cohesive particles and consolidation of the cohesive bed may significantly affect the erosion, deposition, and transport of non-cohesive particles. The interactions between cohesive and non-cohesive particles should be taken into account in the simulation of the mixed sediment transport. A NEST modeling framework of mixed cohesive and non-cohesive sediments is described below.

Model Framework

Sediment is defined to be cohesive if its diameter is less than about 0.01 mm. The model divides the sediment mixture into a suitable number of size classes. Because the size of flocs may change with flow and sediment conditions, the sediment size classes are defined based on the gradation of the dispersed sediment particles rather than the floc gradation. In addition, as it is difficult to solve the details of aggregation and disaggregation processes using multiple size classes for the flocs and a large number of model parameters for each size of cohesive sediment need to be evaluated, only one size class is usually used to represent all cohesive particles in the mixture.

The transport of cohesive sediment is usually treated as suspended load and governed by Equation (15). The sediment deposition rate is determined using Equation (32), where $\omega_{sf,k}$ is the settling velocity, and C_{tk} is the section-averaged sediment concentration. For non-cohesive sediment, the coefficient α_k is called the adaptation coefficient, which is determined using the formula of Armanini and di Silvio (1988) or calibrated by measurement data. For cohesive sediment, α_k is called the deposition probability coefficient (Krone, 1962). It is determined by the formula of Mehta and Partheniades (1975) as given by Equation (33), where $\tau_{bd,\min}$ is the critical bed shear stress below which all sediments are deposited on the bed, $\tau_{bd,\max}$ is the critical bed shear stress above which all sediments remain in suspension yielding a zero deposition rate.

$$D_{bk} = \alpha_k \omega_{sf,k} C_{tk} \tag{32}$$

$$\alpha_k = \begin{cases} 0 & \tau_b > \tau_{bd,\max} \\ 1 - \left(\tau_b - \tau_{bd,\min}\right) \Big/ \left(\tau_{bd,\max} - \tau_{bd,\min}\right) & \tau_{bd,\min} < \tau_b \le \tau_{bd,\max} \\ 1 & \tau_b < \tau_{bd,\min} \end{cases} \tag{33}$$

For non-cohesive sediment, the settling velocity $\omega_{sf,k}$ is determined using a formula of single particle settling velocity, such as Wu and Wang's (2006) formula. For cohesive sediment, Thorn (1981) and others established several empirical formulas for the settling velocity of the flocs. Generally, the settling velocity of the flocs can be determined with the relation given by Wu and Wang (2004b) as described in Equation (34), where ω_f is the

representative settling velocity of the flocs, ω_d is the settling velocity of single particles of the cohesive sediment, K_d, K_s, K_{sa} and K_t are the correction factors accounting for the influences of sediment size, sediment concentration, salinity, and turbulence intensity, respectively.

$$\frac{\omega_f}{\omega_d} = K_d K_s K_{sa} K_t \tag{34}$$

Flocculation intensifies as the sediment size decreases. Following Migniot (1968), Qian (1980), Huang (1981), and Dixit et al. (1982), the correction factor K_d is evaluated as given by Equation (35), where d_k is the diameter of the dispersed cohesive sediment particles, d_r is a reference diameter, and n_d is an empirical exponent. The reference diameter d_r has a range from 0.011 to 0.022 mm based on measured data, and n_d is evaluated between 1.8 and 2.0. Equation (35) is only suitable in the range of $d_k \le d_r$. For $d_k > d_r$, K_d is set to 1.0, which means no flocculation occurs for coarse sediments.

$$K_d = \left(d_r / d_k\right)^{n_d} \tag{35}$$

As sediment concentration increases, the floc settling velocity increases until it reaches a maximum value and then decreases. In analogy to the method of Thorn (1981), K_s is evaluated by Equation (36), where C is the sediment concentration in kg/m^3, n is an exponent ranging from 1 to 2 with a mean value of 1.3, r is an exponent ranging 3 to 5, k_1 and k_2 are coefficients, k is equal to $\left(1+k_1 C_p^n\right)\Big/\left(1-k_2 C_p\right)^r$, and C_p is the sediment concentration at which the maximum settling velocity reaches and varies from 1.5 to 15 kg/m^3 depending on the sediment and water properties.

$$K_s = \begin{cases} 1 + k_1 C^n & 0 < C \le C_p \\ k\left(1 - k_2 C\right)^r & C > C_p \end{cases} \tag{36}$$

As salinity increases, the floc settling velocity increases and approaches to a maximum value. The trend can be approximated by Equation (37), where n_{sa} is an empirical exponent, C_{sap} is the salinity at which the influence of salinity tends to be saturated, and $C_{sa,\min}$ is a small threshold value of salinity above which Equation (37) is valid. According to the investigations of Owen (1970), Huang (1981), and Yue (1983), C_{sap} has a value of about 30 ppt. The exponent n_{sa} is 0.53 based on Huang (1981) data, 0.75 according to Yue (1983), and 0.03 according to Peng (1989). This difference may be because their experiments are in different ranges of salinity.

$$K_{sa} = \begin{cases} \left(C_{sa}/C_{sap}\right)^{n_{sa}} & C_{sa,\min} < C_{sa} \le C_{sap} \\ 1 & C_{sa} > C_{sap} \end{cases} \tag{37}$$

As the flow turbulence increases, flocculation intensifies first and then reduces. By using the experiment of Haralampides et al. (2003), K_t is evaluated using Equation (38), where k_{t1}, n_{t1}, and n_{t2} are empirical coefficients, and τ_p is the threshold bed shear stress at which K_t has the maximum value. Like many other parameters, τ_p depends on the sediment properties

and flow conditions and is about 0.17 N/m^2 in the experiments of Haralampides et al. (2003). The parameters k_{t1}, n_{t1}, and n_{t2} need to be evaluated for different cases.

$$K_t = \begin{cases} 1 + k_{t1}\left(\tau_b / \tau_p\right)^{n_{t1}} & 0 < \tau \le \tau_p \\ \left(1 + k_{t1}\right)\left(\tau_b / \tau_p\right)^{-n_{t2}} & \tau > \tau_p \end{cases} \tag{38}$$

The sediment erosion rate is determined by Equation (39), where p_{bk} is the fraction of the kth size class in the surface layer of bed material, and E_{bk}^* is the potential erosion rate of the kth size class. For non-cohesive sediment, E_{bk}^* is determined using Equation (40), where C_{tk}^* is the potential transport capacity in terms of concentration of bed-material load and is determined using the formula of Wu et al. (2000).

$$E_{bk} = p_{bk} E_{bk}^* \tag{39}$$

$$E_{bk}^* = \alpha_k \omega_{sf,k} C_{tk}^* \tag{40}$$

Cohesive sediment is eroded from the bed either in particles (surface erosion) or in layers (mass erosion). The surface erosion occurs when the applied shear stress exceeds a certain critical shear stress, and mass erosion happens when the applied shear stress exceeds the bulk strength of the sediment. Partheniades (1965) found that the surface erosion rate is a linear function of the dimensionless excess shear stress, while Raudkivi and Hutchison (1974) observed that it is exponentially proportional to the dimensionless excess shear stress. Mehta (1986) clarified that the exponential relation is valid for partially consolidated beds and the linear relationship is valid for fully consolidated beds. For cohesive sediment, E_{bk}^* is determined by Equation (41), where M is a coefficient related to the material properties (such as mineral composition, organic material, and salinity), n is an empirical exponent, and τ_{ce} is the critical shear stress for erosion. The critical shear stress for erosion, τ_{ce}, depends on the mud dry density, organic material, temperature, pH value, the Sodium Absorption Ratio (SAR), etc. Partheniades (1965) found n to be 1. In the study of fine sediment transport in lakes and reservoirs, Gailani et al. (1991) found that the power index n ranges from 2 to 3 and the coefficient M is related to deposition time.

$$E_{bk}^* = M\left(\frac{\tau_b - \tau_{ce}}{\tau_{ce}}\right)^n \tag{41}$$

The critical bed shear stress for surface erosion is significantly affected by consolidation. It increases as the dry bed density increases with time and depth. Thus, the cohesive sediment is more difficult to erode further down the bed layer. Nicholson and O'Connor's (1986) formula, Equation (42), is used to determine τ_{ce} as a function of dry bed density, where ρ_{d0} is the initial dry bed density (kg/m^3), τ_{ce0} is the initial critical shear stress (N/m^2) at ρ_{d0}, k_τ is a coefficient with a value of 0.00037, and n_τ is an exponent given a value of about 1.5.

$$\tau_{ce} = \tau_{ce0} + k_\tau\left(\rho_d - \rho_{d0}\right)^{n_\tau} \tag{42}$$

When non-cohesive and cohesive sediments coexist in the bed material, the incipient motion of non-cohesive sediment may be affected by the cohesion if the fraction of cohesive sediment is larger than a certain value (about 10%). If the fraction of cohesive sediment is

smaller than this value, denoted as $p_{c\min}$, the model sets the critical bed shear stress for non-cohesive sediment the same as that when no cohesive sediment exists. If the cohesive sediment is dominant in the bed, say, the fraction reaches to a certain amount (about 50%) denoted as $p_{c\max}$, the sediment mixture is considered as fully cohesive sediment, i.e., the critical bed shear stress of non-cohesive sediment is equal to that of cohesive sediment. In the case of cohesive sediment fraction between $p_{c\min}$ and $p_{c\max}$, a linear relation between the critical shear stress and the cohesive sediment fraction is assumed. Thus, the critical shear stress of non-cohesive sediment size classes is determined using Equation (43), where $\tau_{ck,n}$ is the critical bed shear stress of the kth size class in the situation where only non-cohesive sediment exists, calculated using the method of Wu et al. (2000) that considers the hiding and exposure effects of non-uniform bed material.

$$\tau_{ck} = \begin{cases} \tau_{ck,n} & p_c < p_{c\min} \\ \tau_{ck,n} + \left(\tau_{ce} - \tau_{ck,n}\right)\dfrac{p_c - p_{c\min}}{p_{c\max} - p_{c\min}} & p_{c\min} \le p_c \le p_{c\max} \\ \tau_{ce} & p_c > p_{c\max} \end{cases} \tag{43}$$

Equation (43) considers the interactions between cohesive and non-cohesive bed sediments. It should be noted that this approach has simplifications and assumptions. More sophisticated approach may be developed. However, the key issue is that there is very little data in the literature regarding such interactions. Laboratory experiments and field investigations are needed to improve the understanding and modeling of this complex phenomenon.

The rate of change in bed sediment mass and the bed material sorting are simulated using the multiple-layer approach presented in the previous chapter. In addition to bed change caused by sediment transport, the bed lowers due to consolidation. The detailed consolidation process can be described by the theory of Gibson et al. (1967). The model based on this theory calculates the evolution of the void ratio of a soil layer using a 1-D unsteady differential equation in the vertical direction. This approach is usually time-consuming. Therefore, a simpler approach is often used, which uses empirical functions to determine the evolution of dry density. The dry bed density increases very rapidly in the first a few days of consolidation, then increases slowly, and finally approaches to the ultimate mean bed density. The model approximates the temporal variation of dry bed density in the first year of consolidation using the modified Hayter (1983) formula as given by Equation (44), where ρ_{d1} is the dry bed density at one-year consolidation time, t is the consolidation time, and a_ρ and p are empirical coefficients.

$$\frac{\rho_d}{\rho_{d1}} = 1 - a_\rho e^{-pt} \tag{44}$$

When the consolidation time is larger than (approximately) one year, the consolidation process is very slow. This long-term temporal variation of dry bed density is calculated using the Lane and Koelzer (1953) formula given by Equation (45), where β is a coefficient. Equations (44) and (45) are applied to only cohesive sediment size classes. For the entire bed material mixture, the dry density is determined by weight-averaging all size classes' values using the Colby (1963) method.

$$\rho_d = \rho_{d1} + \beta \log t \tag{45}$$

To more accurately account for the non-uniformity of bed material in depth, multiple layers can be used to represent the bed material. The change of each layer thickness is determined using Equation (46), where δ_j is the thickness, and ρ_{dj} is the dry density of the jth layer of bed material. Discretization of Equation (46) and summation over all bed layers leads to the overall bed change due to consolidation as given by Equation (47), where J is the total number of the divided bed material layers.

$$\frac{\partial}{\partial t}\left(\delta_j \rho_{dj}\right) = 0 \tag{46}$$

$$\Delta z_{b,c} = \sum_{j=1}^{J}\left(\delta_j^{n+1} - \delta_j^n\right) = \sum_{j=1}^{J}\delta_j^n\left(\frac{\rho_{dj}^n}{\rho_{dj}^{n+1}} - 1\right) \tag{47}$$

Model Test Example

The above model framework has been implemented in the CCHE1D channel network modeling package (Lin, 2010). The resulting sediment transport model has been validated using several laboratory and field cases. One of the field cases was the Lower Fox River in Wisconsin, U.S. Its bed material contains a relatively large percentage of cohesive sediments, which accumulate toxic organic chemicals and heavy metals as a potential contaminant source to Green Bay. The study reach was approximately 11 km long, extended from a dam at the upstream to the river mouth (Figure 16). The East River which joins the Fox River approximately 2 km upstream from the river mouth was considered in the simulation, because its flow discharge was approximately 10% of the main stream discharge (Gailani et al. 1991). A total of 14 cross-sections were assigned to the computational domain, 12 for the main stream and 2 for the tributary. The sediment transport for a 10-year storm event from May 22 to June 20, 1989 was simulated. Figure 17 shows the flow discharges and sediment concentrations at the DePere Dam measured by the USGS and daily water level measured by the National Oceanic and Atmospheric Administration (NOAA), which were used as boundary conditions in the simulation. The time step was 15 min. The Manning's n coefficient was 0.02. Three size classes of 0.00316, 0.0316, and 0.447 mm in diameter were used to represent the fine, medium, and coarse sediments, respectively.

The bed material was divided into three layers. The mixing layer (first layer) and the second layer had the same initial thickness. The top two layers were assumed to constitute a 1-year deposit and the bottom layer was assumed to reflect a 10-year deposit. Various values were used for the mixing layer thickness, and a value 0.002 m was found adequate. The model parameters are shown in Table 1. Figure 18 compares the measured and calculated sediment concentrations at the river mouth. The simulation shows that the calculated sediment concentration reached the peak when the flow was moderate in the early time. The sediment concentration started to decrease even though the flow continued to increase or was kept approximately the same, because the top two layers were eroded away in the early days and the bottom layer was more difficult to erode. The magnitude of the peak sediment concentration and the time to peak were well reproduced by the numerical model.

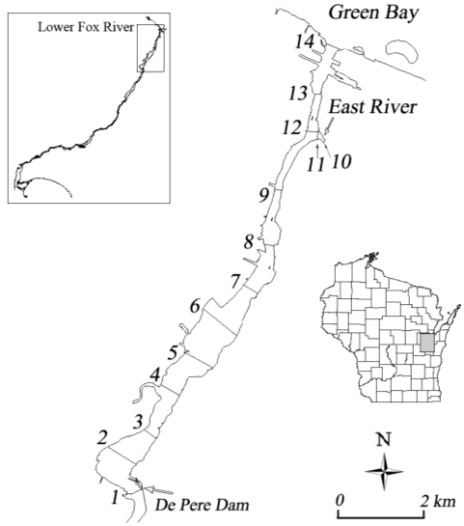

Figure 16. Sketch of the lower Fox River

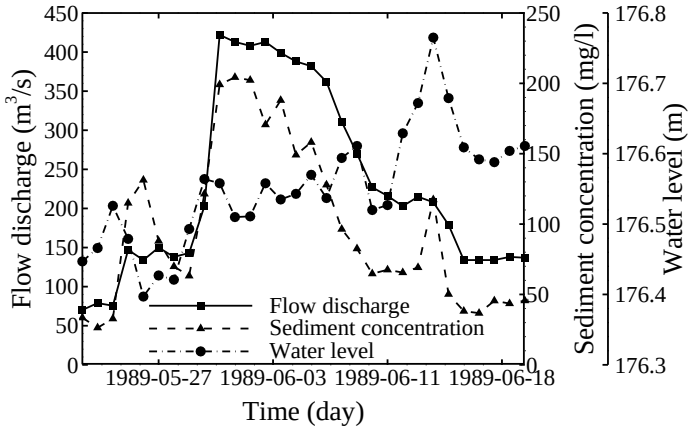

Figure 17. Flow discharge and sediment concentration at Depere Dam and water level at the mouth of the lower Fox River from May 22 to June 20, 1989

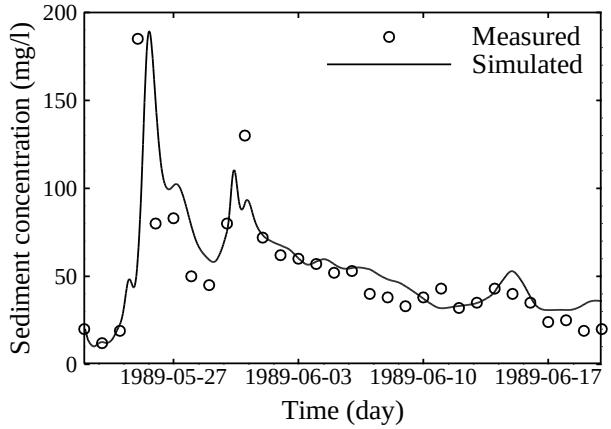

Figure 18. Sediment concentrations at the mouth of the lower Fox River (Lin, 2010)

Table 1. Model parameters used in the lower Fox River case

Settling velocity $\omega_{sf,k}$	K_d	$d_r = 0.012$ mm, $n_d = 1.8$
	K_s	$k_1 = 50.0$, $k_2 = 0.008$, $n = 1.3$, $r = 4.0$, $C_p = 3.5$ kg/m^3
	K_t	$\tau_p = 0.17$ N/m^2, $n_{t1} = 0.165$, $n_{t2} = 0.16$, $k_{t1} = 1.5$
	K_{sa}	1
Deposition probability α		$\tau_{bd,\min} = 0.0$ N/m^2, $\tau_{bd,\max} = \tau_{ce}$
Potential erosion rate E_{bk}^*		M=5.0×10^{-8} m/s, n=2.5, τ_{ce} by Equation (42) with $\tau_{ce0} = 0.01$ N/m^2, $k_\tau = 0.00037$, and $n_\tau = 1.5$
Dry bed density		Equation (45) with $\rho_{d1} = 1489.0$, 1041.0 and 480 kg/m^3 $\beta = 0.0$, 91.0 and 256.0 for sand, silt and clay, respectively

CONCLUSION

The NEST model has been extended and applied to simulate non-cohesive sediment transport induced by rapidly-varying transient flows, by coastal currents and waves, in vegetated water bodies, and by overland flow. In the case of rapidly-varying transient flows, such as dam/levee break flows, storm surge and tsunami waves, the flows may be transcritical, the sediment transport is strong and the bed changes rapidly. Thus, the presented model adopts the generalized shallow water flow equations that consider interactions between flow, sediment transport and bed change, as well as shock-capturing schemes to handle the mixed-regime flows. In the coastal context, the flow model adopts the phase-averaged shallow water flow equations with wave-induced radiation stresses and is coupled with a spectral wave transformation model. The accompanying sediment transport model accounts for sediment entrainment and mixing (diffusion and dispersion) by currents and waves. In vegetated channels and marshlands, the flow model can consider the porosity effect of vegetation and takes into account the vegetation drag and inertia forces in the momentum equations. The associated sediment transport model includes sediment transport capacity affected by vegetation. For soil erosion and transport in upland, a 2-D diffusion wave model is used to simulate the overland flow. The model considers the rainfall, infiltration, and evaporation, and the related sediment transport model takes into account the rill/interrill erosion due to raindrop splash and hydraulic shear. Even though different flow models are used in these cases, the sediment transport models have similar model formulations, which are extensions of the general NEST model described in the previous chapter. The differences in these models arise from evaluation of sediment entrainment, adaptation length, and diffusion coefficient.

A general NEST model framework has been also developed for simulating transport of cohesive/non-cohesive sediment mixtures. It takes into account the effects of cohesive sediment flocculation, bed consolidation and interactions between cohesive and non-cohesive bed materials. Flocculation is considered by determining the floc settling velocity as function

of sediment size, concentration, salinity and turbulent intensity. The critical shear stress of cohesive sediment erosion is related to the dry bed density, which varies with time due to consolidation. The critical shear stress of non-cohesive sediments is corrected when the cohesive fraction exceeds a certain limit, such as 10%. The mixture transport is described using the same transport equation with unified formulas for the erosion and deposition rates of cohesive and non-cohesive sediment size classes. The model framework has been implemented and tested in a 1-D channel network model and can be extended to 2-D and 3-D cases under various flow conditions.

It is well accepted that sediment transport modeling is highly empirical and many model parameters are case dependent. Testing using laboratory and field measurement data has demonstrated that the most important parameters in the NEST models are the sediment transport capacity (or entrainment) formula and the adaption length. Among these two parameters, the sediment transport (or entrainment) capacity formula is more important, because it affects the simulated bed morphology changes both quantitatively and qualitatively. The adaptation length usually affects the simulated bed changes only quantitatively. More laboratory experiments and field measurements are needed to improve the models in different applications.

ACKNOWLEDGEMNTS

The studies presented in this chapter were supported by the USDA Agricultural Research Service, the U.S. Army Corps of Engineers' CIRP program, the USDHS SERRI program and The University of Mississippi.

REFERENCES

Armanini, A., di Silvio, G., (1988). A one-dimensional model for the transport of a sediment mixture in non-equilibrium conditions. *Journal of Hydraulic Research*, IAHR, 26(3), 275–292.

Ashida, K., Michiue, M., (1972). Study on hydraulic resistance and bed-load transport rate in alluvial stream. *Transactions of the Japan Society of Civil Engineers*, 206, 59–69 (in Japanese).

Barfield, B.J., Tollner, E.W., Hayes, J.C., (1979). Filtration of sediment by simulated vegetation, I. Steady-state flow with homogeneous sediment. *Transaction of the American Society of Agricultural Engineers*, 22(3), 540–545.

Barfield, B.J., Barnhisel, R.I., Powell, J.L., Hirschi, M.C., Moore, I.D., (1983). Erodibilities and eroded size distribution of western Kentucky mine spoil and 154 reconstructed topsoil. Final Report for Title III Grant No. G1115211, Institute for Mining and Minerals Research and CRIS Project No. 907-15-2, University of Kentucky, Lexington, KY.

Bennett, S.J., Alonso, C.V., (2003). Physically modeling stream channel adjustment to woody riparian vegetation. American Geophysical Union, Fall Meeting, Abstract #H52A-1171.

Buonaiuto, F.S., Militello, A., (2003). Coupled circulation, wave, and morphology-change modeling, Shinnecock Inlet, New York. Proceedings of the 8th Conference on Estuarine and Coastal Modeling, ASCE, New York, 819–838.

Buttolph, A.M., Reed, C.W., Kraus, N.C., Ono, N., Larson, M., Carmenen, B., Hanson, H., Wamsley, T., Zundel, A.K., (2006). Two-dimensional depth-averaged circulation model CMS-M2D: Version 3.0, Report 2: Sediment transport and morphology change. Coastal and Hydraulics Laboratory Technical Report ERDC/CHL TR-06-9, U.S. Army Engineer Research and Development Center, Vicksburg, MS, U.S.A.

Carmenen, B., Larson, M., (2007). A unified sediment transport formulation for coastal inlet application. Coastal and Hydraulics Laboratory Technical Report ERDC-CHL CR-07-01, U.S. Army Engineer Research and Development Center, Vicksburg, MS, U.S.A.

Cao, Z., Pender, G., Wallis, S., Carling, P,. (2004). Computational dam-break hydraulics over erodible sediment bed. *Journal of Hydraulic Engineering*, ASCE, 130(7), 689–703.

Colby, B.R., (1963). Discussion of Sediment transportation mechanics: Introduction and properties of sediment, Progress report by the Task Committee on preparation of sediment manual of the committee on sedimentation of the hydraulics division, V. A. Vanoni, Chmn., *Journal of the Hydraulics Division*, ASCE, 89(1), 266–268.

Di Giammarco, P., Todini, E., Lamberti, P. (1996). A conservative finite element approach to overland flow: The control volume finite element formulation. *Journal of Hydrology*, 175(1–4), 267–291.

Dixit, J.G., Mehta, A.J., Partheniades, E., (1982). Redepositional properties of cohesive sediments deposited in a long flume. UFL/COEL-82/002, Coastal and Oceanographic Engineering Department, University of Florida, Gainesville, Florida, USA.

Faeh, R., (2007). Numerical modeling of breach erosion of river embankments. *Journal of Hydraulic Engineering*, ASCE, 133(9), 1000–1009.

Gailani, J., Ziegler, C.K., Lick , W., (1991). Transport of suspended solids in the Lower Fox River. *Journal of Great Lakes Research*, 17(4), 479–494.

Gibson, R.E., England, G.L., Hussey, M.J., (1967). The theory of one-dimensional consolidation of saturated clays. *Geotechnique*, 17, 216–263.

Haralampides, K., McCorquodale, J.A., Krishnappan, B.G., (2003). Deposition properties of fine sediment. *Journal of Hydraulic Engineering*, ASCE, 129(3), 230–234.

Harten, A., Lax, P.D., van Leer, B., (1983). On upstream differencing and Godunov-type schemes for hyperbolic conservation laws. *SIAM Review*, 25(1), 35–61.

Hayter, E.J., (1983). Prediction of cohesive sediment movement in estuarial waters. Ph.D. Dissertation, University of Florida, Gainesville, Florida, USA.

He, Z., Wu, W., Wang, S.S.Y., (2009). An integrated two-dimensional surface and three-dimensional subsurface contaminant transport model considering soil erosion and sorption. *Journal of Hydraulic Engineering*, ASCE, 135(12), 1028–1040.

Huang, J.W., (1981). Experimental study of settling properties of cohesive sediment in still water. *Journal of Sediment Res*earch, 2, 30–41 (in Chinese).

IAHR Working Group for Dam-Break Flows over Mobile Beds, (2012). Dam-break flows over mobile beds: Experiments and benchmark tests for numerical models. *Journal of Hydraulic Re*search, IAHR, 50(4), 364–375.

Jordanova, A.A., James, C.S., (2003). Experimental study of bed load transport through emergent vegetation. *Journal of Hydraulic Engineering*, ASCE, 129(6), 474–478.

Karambas, T.V., (2003). Nonlinear wave modeling and sediment transport in the surf and swash zone. *Advances in Coastal Modeling*, V.C. Lakhan (ed.), Elsevier Oceanography Series, 67, Amsterdam, The Netherlands, 267–298.

Krone, R.B., (1962). Flume studies on the transport of sediment in estuarine shoaling processes. Hydraulic Engineering Laboratory, University of Berkeley, California, USA.

Lane, E.W., Koelzer, V.A., (1953). Density of sediments deposited in reservoirs. Report No. 9, A study of methods used in measurement and analysis of sediment loads in streams, Engineering District, St. Paul, MN, USA.

Larson, M., Hanson, H., Kraus, N.C., (2003). Numerical modeling of beach topography change. *Advances in Coastal Modeling*, V.C. Lakhan (eds.), Elsevier Oceanography Series, 67, Amsterdam, The Netherlands, 337–365.

Li, R.M., Shen H.W., (1973). Effect of tall vegetation on flow and sediment. *Journal of the Hydraulics Division*, ASCE, 99(5), 793–814.

Lin, L., Demirbilek, Z., Mase, H., Zheng, J., Yamada, F., (2008). CMS-Wave: A nearshore spectral wave processes model for coastal inlets and navigation projects. Coastal and Hydraulics Laboratory Technical Report ERDC/CHL TR-08-13, U.S. Army Engineer Research and Development Center, Vicksburg, MS, U.S.A.

Lin, Q., (2010). A one-dimensional model of cohesive sediment transport in open channels. MS Thesis, The University of Mississippi, USA.

Lopez, F., Garcia, M., (2001). Mean flow and turbulence structure of open-channel flow through non-emergent vegetation. *Journal of Hydraulic Engineering*, ASCE, 127(5), 392–402.

Low, H.S., (1989). Effect of sediment density on bed-load transport. *Journal of Hydraulic Engineering*, ASCE, 115(1), 124–138.

Mehta, A.J., (1986). Charaterization of cohesive sediment properties and transport processes in estuaries. In Estuarine Cohesive Sediment Dynamics, A.J. Mehta (ed.), Springer-Verlag, 290–325.

Mehta, A.J., Partheniades, E., (1975). An investigation of the depositional properties of flocculated fine sediment. *Journal of Hydraulic Research*, IAHR, 13(4), 361–381.

Migniot, C., (1968). A study of the physical properties of different very fine sediments and their behavior under hydrodynamic action. *La Houille Blanche*, 7, 591–620. (in French)

Morison, J.R., O'Brien, M.P., Johnson, J.W., Schaaf, S.A., (1950). The force exerted by surface waves on piles. *Petroleum Transactions*, American Institute of Mining Engineers, 189, 149–154.

Morris, M.W., Kortenhaus, A., Visser, P.J., (2009). Modelling breach initiation and growth. FLOODsite Report T06-08-02, FLOODsite, www.floodsite.net

Nicholson, J., O'Connor, B.A., (1986). Cohesive sediment transport model. *Journal of Hydraulic Engineering*, ASCE, 112(7), 621–639.

Nikora, V., McEwan, I., McLean, S., Coleman, S., Pokrajac, D., Walters R., (2007). Double-averaging concept for rough-bed open-channel and overland flows: Theoretical background. *Journal of Hydraulic Engineering*, 133(8), 873–883.

Okabe, T., Yuuki, T., Kojima, M., (1997). Bed-load rate on movable beds covered by vegetation. Proc. 27th Congress of IAHR, San Francisco, USA, 2, 809–814.

Owen, M.W., (1970). A detailed study of the settling velocities of an estuary mud. Report No. INT 78, Hydraulics Research Station, Wallingford, UK.

Partheniades, E., (1965). Erosion and deposition of cohesive soils. *Journal of the Hydraulics Division*, ASCE, 91(HY1), 105–139.

Peng, R.Z., (1989). Experimental study on flocculation fall of sediment particles in Yangtze estuary. Technical Report, IWHR, Beijing, China.

Qian, Y.Y., (1980). Basic properties of hyper-concentrated flow. Proc. First International Symposium on River Sedimentation, Beijing, China.

Raudkivi, A.J., Hutchison, D.L., (1974). Erosion of kaolinite clay by flowing water. *Proceedings The Royal Society London*, Series A, 337, 537–544.

Richardson, J.F., Zaki, W.N., (1954). Sedimentation and fluidisation, Part I. *Transactions of the Institution of Chemical Engineers*, 32(1), 35–53.

Roelvink, D., Reniers, A., van Dongeren, A., de Vries, J.V.T., McCall, R., Lescinski, J., (2009). Modelling storm impacts on beaches, dunes and barrier islands. *Coastal Engineering*, Elsevier, 56, 1133–1152.

Rosati, J.D., Gravens, G.W., Smith, M.B., (1999). Regional sediment budget for Fire Island to Montauk Point, New York, USA. Proceedings Coastal Sediments ’99, N.C. Kraus and W.G. McDougal (eds.), ASCE, Reston, VA, 802–817.

Sanchez, A., Wu, W., (2011). A non-equilibrium sediment transport model for coastal inlets and navigation channels. *Journal of Coastal Research*, Special Issue, 59, 39–48.

Sanchez, A., Wu, W., Beck, T.M., Li, H., Rosati, J.D., Demirbilek, Z., Brown, M., (2011). Verification and validation of the Coastal Modeling System, Report 4: Sediment transport and morphology change. ERDC/CHL TR-11-10, Coastal and Hydraulics Laboratory, U.S. Army Engineer Research and Development Center, Vicksburg, MS.

Soulsby, R.L., (1997). Dynamics of marine sands, a manual for practical applications. Thomas Telford Publications, London, England.

Struiksma, N., Olewesen, K.W., Flokstra, C., de Vriend, H.J., (1985). Bed deformation in curved alluvial channels. *Journal of Hydraulic Research*, 23(1), 57–79.

Thorn, M.F.C., (1981) Physical processes of siltation in tidal channels. Proceedings, Hydraulic Modelling Applied to Maritime Engineering Problems, ICE, London, England, 47–55.

Toro, E.F., (2001). Shock-capturing methods for free-surface shallow flows, Wiley.

van Leer, B., (1979). Towards the ultimate conservative difference scheme. V. A second order sequel to Godunov's method. *Journal of Computational Physics*, 32(1), 101–136.

van Rijn, L.C., (1984a). Sediment transport, part I: Bed load transport. *Journal of Hydraulic Engineering*, ASCE, 110(10), 1431–1456.

van Rijn, L.C., (1984b). Sediment transport, part II: Suspended load transport. *Journal of Hydraulic Engineering*, ASCE, 110(11), 1613–1641.

van Rijn, L.C., (2007a). Unified view of sediment transport by currents and waves. I: Initiation of bed motion, bed roughness, and bed-load transport. *Journal of Hydraulic Engineering*, 133(6), 649–667.

van Rijn, L.C., (2007b). Unified view of sediment transport by currents and waves. II: Suspended transport. *Journal of Hydraulic Engineering*, 133(6), 668–689.

Wang, Z., Bowles, D.S., (2006). Three-dimensional non-cohesive earthen dam breach model. Part 1: theory and methodology. *Advances in Water Resources*, 29, 1528–1545.

Watanabe, A., (1985). Three-dimensional predictive model of beach evolution around a structure. Proceedings of the International Symposium of Water Wave Research. University of Hannover, Germany, 121–142.

Watanabe, A., (1987). 3-dimensional numerical model of beach evolution. Proceedings Coastal Sediments ’87, N.C. Kraus (ed.), ASCE, Reston, VA, 802–817.

Wu, W., (2007). Computational River Dynamics, Taylor & Francis, London, U.K.; Balkema, Leiden, The Netherlands.

Wu, W., He, Z., (2009). Effects of vegetation on flow conveyance and sediment transport capacity. *International Journal of Sediment Research*, 24(3), 247–259.

Wu, W., Lin, Q., (2012). Nonuniform sediment transport under current and waves. *Proc. 33rd Int. Conf. on Coastal Engineering*, Santander, Spain.

Wu, W., Marsooli, R., (2012). A depth-averaged 2-D shallow water model for breaking and non-breaking long waves affected by vegetation. *Journal of Hydraulic Research*, IAHR, In press.

Wu, W., Marsooli, R., He, Z., (2012). A depth-averaged two-dimensional model of unsteady flow and sediment transport due to non-cohesive embankment break/breaching. *Journal of Hydraulic Engineering*, ASCE, 138(6), 503–516.

Wu, W., Shields, F.D.Jr., Bennett, S.J., Wang, S.S.Y., (2005). A depth-averaged 2-D model for flow, sediment transport and bed topography in curved channels with riparian vegetation. *Water Resources Research*, AGU, 41, W03015.

Wu, W., Wang, S.S.Y., (2004a). Depth-averaged numerical modeling of flow and sediment transport in open channels with vegetation. Riparian vegetation and fluvial geomorphology, S. J. Bennett and A. Simon (eds.), American Geophysics Union, USA.

Wu, W., Wang, S.S.Y., (2004b). Depth-averaged 2-D calculation of tidal flow, salinity and cohesive sediment transport in estuaries. *International Journal of Sediment Research*, 19(3), 172–190.

Wu, W., Wang, S.S.Y., (2006). Formulas for sediment porosity and settling velocity. *Journal of Hydraulic Engineering*, ASCE, 132(8), 858–862.

Wu, W., Wang, S.S.Y., (2007). One-dimensional modeling of dam-break flow over movable beds. *Journal of Hydraulic Engineering*, ASCE, 133(1), 48–58.

Wu, W., Wang, S. S. Y. and Jia, Y., (2000). Nonuniform sediment transport in alluvial rivers. *Journal Hydraulic Research*, IAHR, 38(6), 427–434.

Wu, W., Sanchez, A. and Zhang, M., (2011). An implicit 2-D shallow water flow model on unstructured quadtree rectangular mesh. *Journal of Coastal Research*, Special Issue, (59), 15–26.

Xiang, H., (2002). Studies on the runoff and sediment yield for complex hillslopes. MS Thesis, Institute of Mechanics, Chinese Academy of Sciences, Beijing.

Yalin, M.S., (1963). An expression for bed-load transportation. *Journal of the Hydraulics Division*, ASCE, 89(3), 221–248.

Ying, X., Wang, S.S.Y., (2008). Improved implementation of the HLL approximate Riemann solver for one-dimensional open channel flows. *Journal of Hydraulic Research*, IAHR, 46(1), 21–34.

Yue, P.J., (1983). Preliminary study of flocculation formed by cohesive sediment and its influence on rheologic properties of slurry. *Journal of Sediment Res*earch, 1, 25–35 (in Chinese).

Ziegler, C.K., Nisbet, B.S., (1995). Long-term simulation of fine-grained sediment transport in large reservoir. *Journal of Hydraulic Engineering*, ASCE, 121(11), 773–781.

Zhu, J., (1991). A low diffusive and oscillation-free convection scheme. *Communication in Applied Numerical Methods*, 7, 225–232.